A novel offline robust trajectory optimization index and method for underground mining cable-driven parallel robot

Jia, Weihan; Cheng, Gang; Li, Jun; Pang, Yusong; Hu, Mengyao; Gu, Wei

DOI
10.1016/j.mechmachtheory.2025.106095

Publication date
2025

Document Version
Final published version

Published in
Mechanism and Machine Theory

Citation (APA)
Jia, W., Cheng, G., Li, J., Pang, Y., Hu, M., & Gu, W. (2025). A novel offline robust trajectory optimization index and method for underground mining cable-driven parallel robot. *Mechanism and Machine Theory*, *214*, Article 106095. https://doi.org/10.1016/j.mechmachtheory.2025.106095

Mechanism and Machine Theory 214 (2025) 106095

Contents lists available at ScienceDirect

Mechanism and Machine Theory

journal homepage: www.elsevier.com/locate/mechmt

Research paper

A novel offline robust trajectory optimization index and method for underground mining cable-driven parallel robot

Weihan Jia [a], Gang Cheng [a,*], Jun Li [a], Yusong Pang [b], Mengyao Hu [a], Wei Gu [c]

[a] *Faculty of Mechanical Engineering, China University of Mining and Technology, Xuzhou 221116, China*
[b] *Faculty of Mechanical Engineering, Delft University of Technology, Delft 2628, the Netherlands*
[c] *Shandong Zhongheng Photoelectric Technology Co. LTD, Zaozhuang 277020, China*

ARTICLE INFO

Keywords:
Cable-driven parallel robot
Robust optimal stiffness direction
Offline trajectory optimization method
Multiple trajectories evaluation mechanism
Stiffness model correction

ABSTRACT

The stiffness model plays a crucial role in improving the performance of robots. During the operation of an underground mining cable-driven parallel robot (UMCDPR), insufficient stiffness can lead to motion instability, posing safety hazards. Additionally, the complexity of the underground mining environment, which is often accompanied by external disturbances, leads to offline stiffness indices failing when used underground as an optimal criterion. To address these problems, this article proposes a robust optimal stiffness direction (ROSD) index grounded in Rayleigh's theorem, which is characterized by three primary features: (1) strong robustness, (2) suitable for multi-trajectory optimization engineering problems, and (3) global visualization. Firstly, considering the influence of pulleys on the end-effector, the stiffness model of UMCDPR is modified. Secondly, a trajectory optimization method utilizing ROSD is introduced, incorporating the Kepler Conjecture and stiffness model correction. Finally, the characteristics of ROSD are validated through numerical simulations. Based on two numerical simulations, the ROSD index can serve as an optimal criterion for guiding stiffness optimization of UMCDPR. Furthermore, an optimal stiffness trajectory is obtained to meet the task objectives of UMCDPR.

1. Introduction

In 2020, China's raw coal output amounted to 3.84 billion tons, while its total coal consumption approximated 4.14 billion tons [1]. According to research on China's coal resources, underground mining is the principal extraction method, with opencast mining comprising less than 15 % of overall coal production [2]. Notably, underground mining offers several substantial advantages, including the reduction of transportation costs, the enhancement of mining efficiency, and the mitigation of labor intensity. These factors collectively underscore the significance of underground mining in the context of China's coal industry.

Hydraulic supports are mainly transported by cranes on the ground as pivot equipment for fully mechanized mining. Assembling the equipment underground assists in reducing transportation and operational costs. Nonetheless, traditional cranes, due to their weight and size, are unsuitable for underground operations. Cable-driven parallel robots (CDPRs) are characterized by high speed, high stiffness, high loading capacity, high flexibility, and high motion accuracy [3,4]. Their potential advantages allow them to replace large lifting devices for accomplishing underground tasks, enabling them to adapt to more complex environments and fulfill various task requirements. Therefore, it is imperative to select an appropriate technology to develop UMCDPR to ensure the transport of

---

* Corresponding author.
E-mail address: chg@cumt.edu.cn (G. Cheng).

https://doi.org/10.1016/j.mechmachtheory.2025.106095
Received 6 November 2024; Received in revised form 26 April 2025; Accepted 28 May 2025

hydraulic supports in the limited space of underground mines.

UMCDPR is susceptible to external disturbances in the complex underground environment, resulting in motion instability and triggering potential safety incidents. Having great stiffness can assist UMCDPR in withstanding underground disturbances during its operation. One of the current research hotspots is how to evaluate the stiffness of robots. Cui et al. [5] defining a new cable tension constraint workspace concept to analyze and measure the controllability of the overall and local stiffness of CDPRs. Yu et al. [6] proposing a stability factor to evaluate the stability of CDPRs. Following this requirement, a feasible workspace and an SFW generation algorithm are presented based on convex set theory. Jamshidifar et al. [7] propose the cables' tension redundancy problem. Redundancy resolution is studied considering the directional stiffness of the moving platform as the objective function to maximize. Yuan et al. [8] analyze the dynamic and static stiffness of CDPRs by considering the mass of the cables, revealing that the mass of cables significantly impacts the stiffness of CDPRs. Unfortunately, most scholars predominantly concentrate on the system stiffness of CDPRs, neglecting that the stiffness index used to reflect CDPR systems is only valid within a certain range of external disturbances, while becoming invalid beyond this range. This issue is particularly prominent in underground environments.

UMCDPR is a novel underground mining equipment that requires remarkable safety, reliability, and economy before being put into production. Nonetheless, directly developing an online control system is not a smart choice. On the one hand, given the inability to accurately estimate underground disturbances (including mutual influence between workshops [9] and rock layer movements [10]), online control is difficult to execute accurately when disturbances are not accurately estimated [11]. On the other hand, novel online algorithms must be redeveloped to meet the explosion-proof requirements of different underground environments, and the longer cycle increases the cost of use [12]. Therefore, offline simulations are employed to select a direction with minimal deformation for UMCDPR trajectory planning to increase stiffness performance. Due to the presence of underground disturbances causing the indices to fail, there is a significant discrepancy between offline simulation planning and actual online planning. One effective solution is to improve the robustness of the index [13,14]. In this article, the disturbance boundary value that exactly does not cause the indices to fail is defined as the disturbance capacity. Meanwhile, offline analysis based on stiffness optimization index is a commonly used method in many works [5–8]. According to the compliance/stiffness ellipse mechanism [15,16], alterations in the robot's motion direction induce variations in system stiffness. Meanwhile, motion direction is also related to the robot's task trajectory. In other words, appropriate motion trajectory planning can effectively enhance the stiffness of CDPRs. To the authors' knowledge, most existing researches focus on optimizing CDPRs' motion stiffness from the perspective of cable tension distribution [5–8], while overlooking CDPRs' actual task trajectories. This article proposes a novel approach by enhancing the system's stiffness performance through directional optimization that aligns motion direction with task requirements, thereby achieving more effective stiffness for CDPRs.

Trajectory planning is a necessary means for CDPRs to achieve task objectives, and reasonably setting path information enhances the working efficiency of CDPRs. Trajectory optimization is performed offline to enhance CDPR performance, allowing it to satisfy or exceed the expected goals. Cheng et al. [17] presenting an optimal trajectory planning control method to suppress the vibration of a variable-stiffness flexible manipulator considering the rigid-flexible coupling. Zhao et al. [18] propose a method of constructing the hybrid stiffness index to enhance the stiffness of the serial robot in completing friction stir welding tasks. Posa et al. [19] present a novel method for trajectory planning of rigid body systems that contact their environment through inelastic impacts and Coulomb friction, eliminating the requirement for a priori mode ordering. In fact, the core elements of trajectory optimization are the optimization indices from the authors' perspectives. Generally, the optimization indices are converted into mathematical equations and optimized through appropriate methods. Such as reducing energy consumption [20], minimizing operational time [21], enhancing the force-feasible workspace [22], motion/force transmissibility [23], available wrench set robustness [16], load capacity indices [24] and performance evaluation for other parallel robots [25,26]. However, for certain engineering problems, the requirements are relatively vague and lack a clear definition [27]. According to the task requirements (transporting a load between two areas) of UMCDPR, there are multiple options for initial and final points of trajectories within a narrow tunnel. Currently, no suitable method exists for selecting an optimal stiffness trajectory from multiple possible trajectories. Therefore, evaluating the optimization results obtained from multiple initial point selections is also one of the problems to be addressed in this article. Furthermore, visualization in optimization is regarded as a crucial means to mitigate local optima [28]. Once the global optimization results of UMCDPR within the task workspace are established, it significantly reduces the difficulty for users in utilizing the methods, facilitating promotion and application in the future.

Nomenclature	
k_{pi}	the modified stiffness model coefficient of the i-th cable
$\overline{k}_{pi}$	the modified stiffness model constant of the i-th cable
TW_t	the optimized task workspace based on the k_{pi}
TW	the task workspace before optimization.
$\boldsymbol{K}_1$	the modified controllable stiffness matrix
$\boldsymbol{K}_2$	the modified inherent stiffness matrix
$\boldsymbol{K}_p$	the modified stiffness matrix of UMCDPR systems
$\boldsymbol{\tau}_{p,\,j,\,min}$	the optimal position stiffness direction at the j-th point
$\boldsymbol{\tau}_{\Phi,j,min}$	the optimal rotation stiffness direction at the j-th point
$\boldsymbol{p}_j$	the position vector at the j-th point
$\boldsymbol{p}_{j+1}$	the position vector at the j+1-th point
$\boldsymbol{\tau}_{j,min}$	the optimal stiffness direction located at $\boldsymbol{p}_j$
Δt	the sampling time

(*continued on next page*)

(*continued*)

δ	the radius of the unit sphere
$\boldsymbol{a}_j$	the direction of movement from $\boldsymbol{p}_j$ to $\boldsymbol{p}_{j+1}$.
$\boldsymbol{a}_n$	the n-th search/motion direction from search/motion direction space

For CDPRs, choosing the cable tension from the wrench feasible workspace (WFW) is an effective method to improve controllable stiffness [29]. This is achieved by aligning the eigenvector associated with the maximum eigenvalue of the stiffness matrix, thereby ensuring significant stiffness in the direction of motion [30]. The eigenvectors corresponding to the eigenvalues of the stiffness/compliance matrix can serve as a standard of stiffness, with an important index being the stiffness/compliance ellipsoid [15,[16]. When the stiffness/compliance ellipsoid is defined, the longer/shorter length of its semi-axes (eigenvalues of the stiffness/compliance matrix), the smaller deformation under force in the corresponding direction (corresponding to the eigenvector), indicating better stiffness performance. The authors can further infer that the optimal stiffness direction of UMCDPR can be determined at any generalized coordinate by changing the eigenvalue of the stiffness/compliance matrix. Hence, choosing the eigenvector corresponding to the minimum or maximum eigenvalue as the optimal stiffness direction is indeed an effective means. To the best of the author's knowledge, there is no literature providing theoretical proof for the existence of the optimal stiffness direction. This article serves as a pioneering work, combining Rayleigh's theorem to demonstrate the existence of the optimal stiffness direction. This method of the optimal direction not only enhances the visualization of stiffness indices but also takes into account the global distribution of ROSD in the task workspace.

In summary, considering the underground environment of UMCDPR, a stiffness optimization index is proposed to ensure the credibility of the results during offline simulation, especially when there are significant differences in disturbances compared to actual experiments. The main contributions of our work can be summarized as follows:

(1) **ROSD index:** This article proposes the ROSD to address the issue of index failure caused by the mismatch between offline simulations and actual experimental disturbances. Numerical simulations are designed to verify the direction similarity under different disturbance means, demonstrating the robustness of this index;
(2) **Multi-trajectory evaluation mechanism:** For the multi-trajectory optimization problem of UMCDPR, a multi-trajectory evaluation system is established based on the ROSD index. The main objective is to select an optimal stiffness motion trajectory from all possible trajectories as the motion trajectory of UMCDPR;
(3) **Global visualization:** According to the generalized coordinates of UMCDPR, it is straightforward to obtain the global distribution of ROSD in the task workspace. When the global distribution of ROSD is observed, this approach facilitates user utilization and helps avoid getting trapped in local optima.

The remainder of this article is organized as follows. In Section 2, an overview of preparatory work on UMCDPR is presented. In Section 3, the ROSD index is proposed by Rayleigh's theorem. Subsequently, an approximation segmentation method of the task workspace is obtained by applying the Kepler Conjecture as the foundational theory, and the ROSD offline trajectory optimization method is proposed with the principle of maximizing the similarity value. In Section 4, both numerical simulations are conducted to verify the correctness of the properties of ROSD, and the mean similarity is introduced into ROSD, from which a trajectory with a maximum deformation no exceeding 0.027 m is obtained to achieve the task objectives. In Section 5, conclusions and future work are presented.

2. Preliminaries

As a precursor to the subsequent sections, this section briefly introduces backgrounds, task objectives, UMCDPR structure, kinematic modelling, and the design of TW. Besides, this section provides explanations of some concepts about ROSD.

2.1. Background and task objectives

The hydraulic support serves as the pivotal equipment for fully mechanized mining faces, capable of adjusting its height according to the thickness of coal seams to safeguard the working conditions within the roadway [31,32] (Fig. 1(a)). The hydraulic support is mainly composed of several parts: front beam, top beam, shield beam, rear linkage, front linkage, base, and support legs (Fig. 1(b)). All of these components can be disassembled for transportation to the underground for assembly.

The mining hydraulic frame structure is commonly utilized for underground lifting and transportation of hydraulic supports (Fig. 1 (c)). It primarily consists of a lifting unit and an elevating unit, and is renowned for its strong load-bearing capacity, high flexibility, and ease of access to the underground. However, compared to chain drives, the UMCDPR offers superior controllable stiffness and control accuracy, as well as a higher safety factor. Therefore, we retain the elevating unit and replace the lifting unit with a cable-driven unit. To a certain extent, the adoption of a mining hydraulic frame needs collaboration with humans. When UMCDPR attains sufficient trajectory stiffness, it can effectively safeguard personal safety and enhance stability (Fig. 1(c)). Therefore, UMCDPR is designed based on the structural characteristics of the mining hydraulic frame. Its structure comprises three parts: a dual cable-driven winch, a pulley system, and a hoisting component (Fig. 1(d)), and is introduced in detail in Section 2.2.

Typically, hydraulic support components are equipped with lifting holes, enabling hooks to be directly connected to these holes.

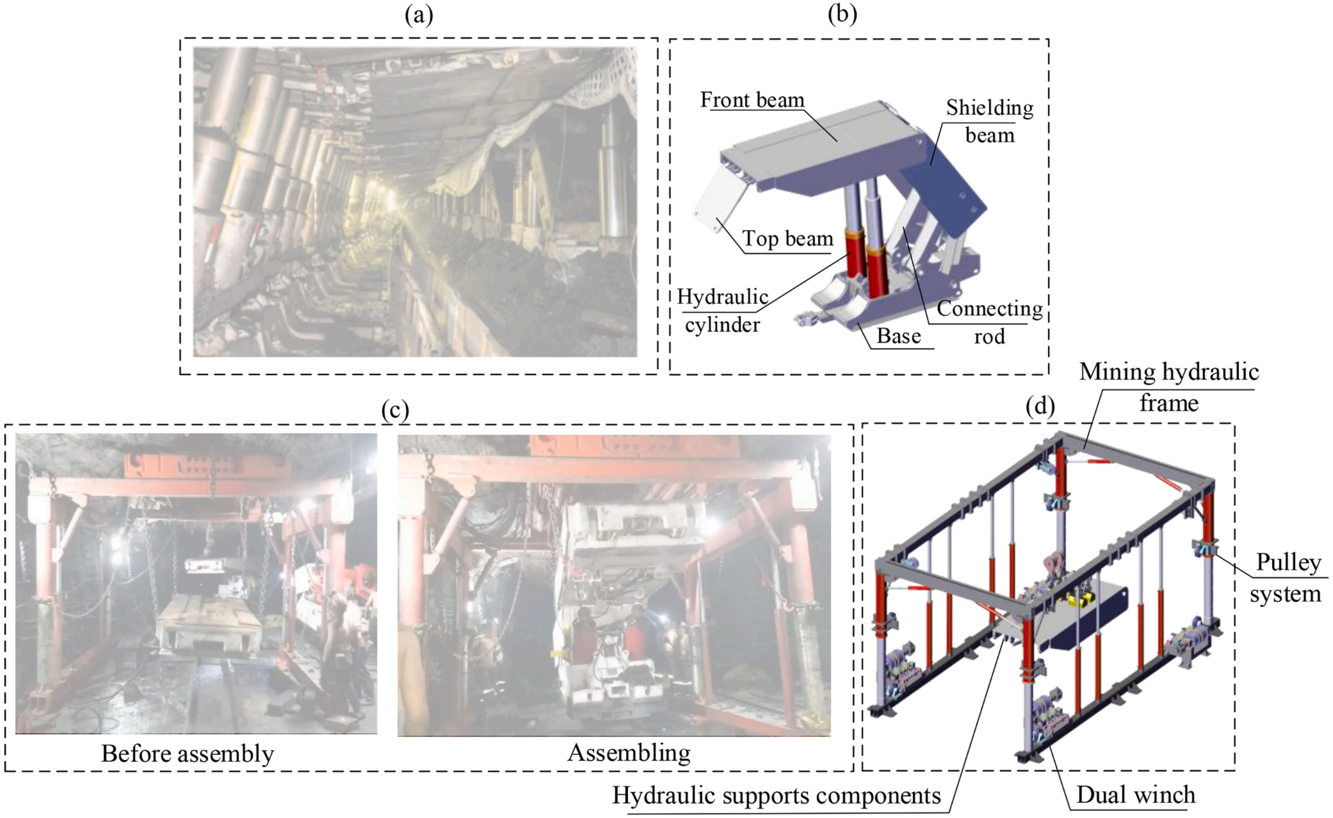

Fig. 1. (a) Hydraulic supports mining faces; (b) Composition of hydraulic support; (c) Mining hydraulic frame working drawing; (d) UMCDPR schematic.

However, prolonged exposure of the lifting hole to heavy loads can cause severe wear, and since it is a part of the hydraulic support and cannot be replaced, it results in a decrease in UMCDPR model accuracy. The permanent magnetic lifter boasts a strong adsorbing force, with a maximum individual capacity to hold objects weighing up to 6000 kg, and it is easy to install and replace. Hence, we utilize four permanent magnetic lifters to mount onto the hydraulic support components, thereby constructing the end-effector in conjunction with the hydraulic support. To minimize swinging during lifting, after determining the center gravity of hydraulic support components through the suspension method during installation, we position it within a rectangle formed by the centers of four permanent magnetic lifters (The area enclosed by a cube is defined as the suitable installation area), thereby enhancing the stability of the load during movement (Fig. 2(a)). Meanwhile, most of the components of hydraulic supports are cylindrical, elongated, or flat in shape. Under conditions of low speed and heavy loading, the torque experienced by the end effector is minimal and hardly considered. Therefore, we can consider the UMCDPR as redundant [33,34]. A reasonable assumption is proposed to facilitate subsequent analysis.

Assumption 1. In an ideal state, the speed is relatively low, allowing the end-effector to consider the hoisting component with 3-DOF translation. This state represents the quasi-static state of UMCDPR.

Based on these background descriptions, UMCDPR primarily has two task objectives.

Establishing stiffness index under disturbance via offline methods: When the end-effector is subjected to strong disturbances, it can lead to the failure of offline indices, resulting in significant discrepancies in experimental outcomes. Consequently, this may lead to unsafe displacement of the end-effector, triggering various potentially unsafe phenomena such as colliding mining hydraulic frames or humans. Therefore, our first objective is to propose a robust optimization criterion that can guide the expected experimental results through offline optimization.

Selecting the optimal trajectory from multi-trajectory: This research mainly focuses on the transportation situation of UMCDPR in a workspace. Before standardizing the assembly process, the UMCDPR is only responsible for transporting loads from one assembling area to another. At this stage, the task objectives lack fixed initial points, terminal points, and explicit motion direction, which renders optimization particularly challenging to achieve. Therefore, our second objective is to select an optimal movement trajectory that is crucial to normalizing the underground assembly process and ensuring personal safety (Fig. 2(b)).

In brief, our total objective is to transport the hydraulic support components between two assembling areas and to select the optimal trajectory with the best stiffness among the possible multi-trajectory.

2.2. Underground mining cable-driven parallel robot

UMCDPR mainly consists of a dual cable-driven winch, a pulley system, a hook, an end-effector, and a mining hydraulic frame (Fig. 3). It is characterized by its simple structure and low cost. The legend for Fig. 3 is shown in Fig. 3(e). Below is a detailed introduction of each component:

Dual cable-driven winch: The dual cable-driven winch includes dual reels, a redirect pulley, an explosion-proof motor, a synchronous belt, and a wiring mechanism (Fig. 3(a)). There are four of them in the UMCDPR system, evenly fixed on both sides of the mining hydraulic frame. Once the motor is activated, the dual reels rotate, causing the wiring mechanism to move along the x-axis to ensure a uniform cable layout on the dual reels [35]. Then, the direction of the cable is changed by the redirect pulley so that it enters the guide pulley. It’s worth noting that when installing the dual cable-driven winch, the channels of the two redirect pulleys need to be aligned with those of the guide pulley.

Pulley system: The pulley system comprises a swivel pulley, a tension pulley, and a guide pulley. The guide pulley primarily directs the cables from the winch and alters the direction in which the cables enter the tension pulley, allowing the tension pulley to effectively tighten the cables and improve the system stiffness performance. When installing the pulley system, first adjust the positions of the four guide pulleys as required and then fix them onto the mining hydraulic frame, ensuring that the dual cables extend along the x-axis. The tension pulley can reduce the loss of tension in the cable during the operation of UMCDPR and increase the rolling friction of cables. When installing the tension pulley, ensure that the mounting plane of the guide pulley and the tension pulley coincide (Fig. 3(a)), which can reduce friction between the cable and the edges of the pulleys, thereby enhancing the lifespan of both the pulleys and cable. The pose of the hoisting component can determine the angle of the swivel pulley, and its cable hole structure allows the cable to enter the swivel pulley from a fixed position (Fig. 3(d)) [36]. The rotational axis of the swivel pulley lies on its plane of symmetry. When installing the swivel pulley, it should be ensured that the rotation axis aligns with the z-axis and the rotation angle remains between -90° and 90°. The pressing device of the swivel pulley ensures that the cable enters through the fixed cable hole, which can reduce the complexity of kinematic modeling.

Hook and cable trend: UMCDPR employs a single, double-stranded cable connected to the end-effector through a hook, enhancing the cables’ load-bearing capacity, system stiffness, and cable utilization efficiency (Fig. 3(b)). The hook adopts a pulley form for connection with the cable, facilitating easy replacement and enhancing stability (Fig. 3(c)). The inner side of the hook is equipped with a fender plate to prevent the cable from detaching from the hook, thereby enhancing the safety of UMCDPR. When installing UMCDPR, first secure both ends of a cable onto dual reels, route it around the redirect pulley, and then pass it through the dual channels of the guide pulley and tension pulley in sequence. Then, it enters the pressing device to prevent the cable from becoming dislodged from the swivel pulley end during the movement of UMCDPR, which could lead to safety issues. Finally, the cable forms a loop around the pulley of the hook (Fig. 3(c)). To make the kinematic model more general and facilitate subsequent research, the two cables are seen as a single unit.

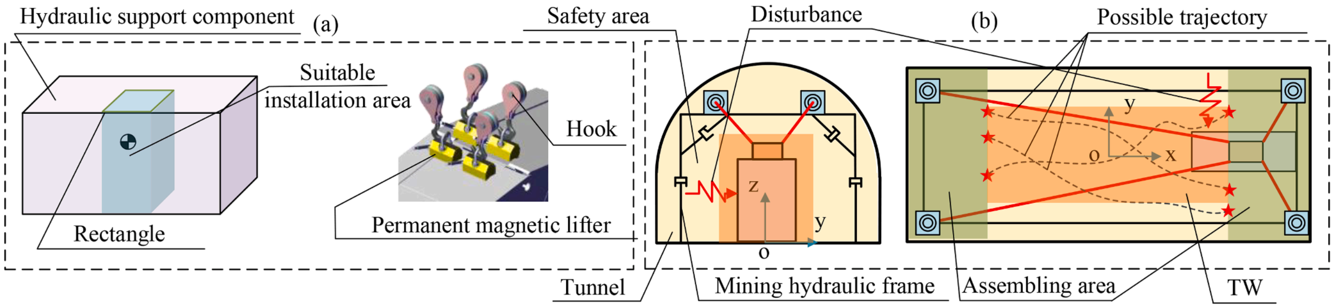

Fig. 2. (a) Hydraulic support connection and installation: The gravity center of the load should be maintained within a rectangular area formed by four permanent magnetic lifters. The green rectangle represents the area enclosed by the centers of four permanent magnetic lifters. (b) Possible trajectories during lifting: The green area in the figure represents the assembling area. The orange area is the task workspace, which is also the working area for UMCDPR. The yellow area is the safety area.

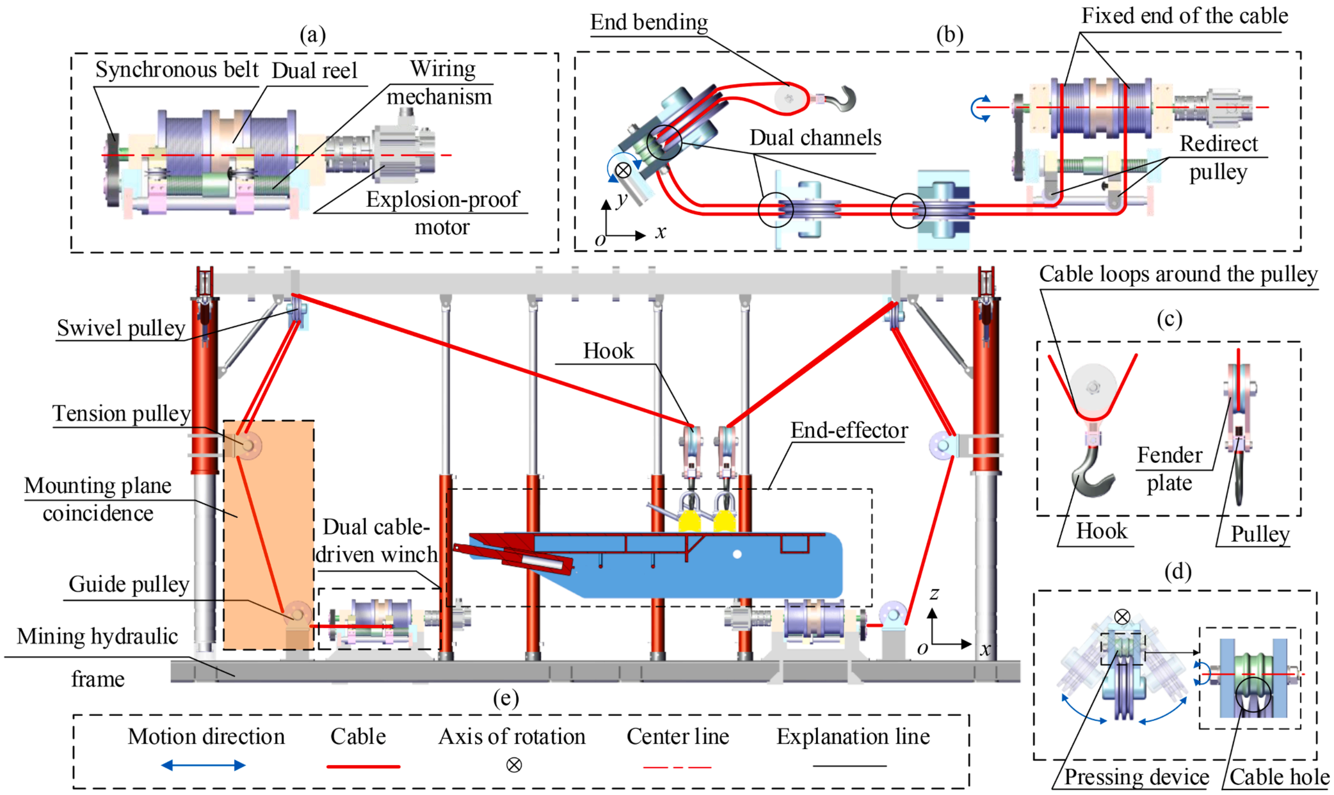

Fig. 3. Profile schematic of UMCDPR. (a) Schematic of the dual cable-driven winch components; (b) Cable trend Schematic; (c) Schematic of the hook connected to the cable; (d) Details of the swivel pulley; (e) Legend of Fig. 3.

2.3. Kinematics

Kinematics is the foundation for the analysis of the stiffness model. To establish the static stiffness model of UMCDPR, the kinematic modelling of UMCDPR is first analyzed. It is well-known that the swivel pulley is a factor influencing the positional kinematics of UMCDPR [37,38]. Although UMCDPR has no extremely high requirements for positional accuracy based on the multi-trajectory task objective (It is fully feasible for UMCDPR to stop either inside or at the edge of the assembly area), it has requirements for UMCDPR speed. Eq. (4) establishes the basic formula for static stiffness [5]. When the velocity of the UMCDPR is excessively fast, it also impacts the static stiffness model, resulting in model failure and causing the UMCDPR to deviate from the quasi-static state. The extent of this influence requires further research. Therefore, Sections 2.3 and 2.4 further explore the extent to which the swivel pulley affects velocity kinematics.

The kinematic model of UMCDPR is shown in Fig. 4(a). The global coordinate system *O-xyz* is fixed on the ground, while the moving coordinate system $P\text{-}x_py_pz_p$ is fixed on the end-effector. Therefore, the generalized coordinate is $\boldsymbol{\varepsilon} = [\boldsymbol{p}^T, \boldsymbol{\Phi}^T]^T$, where the position vector is $\boldsymbol{p} = [x, y, z]^T$ and $\boldsymbol{\Phi} = [\theta_x, \theta_y, \theta_z]^T$. A_i is the center of the swivel pulley rotation axis. B_i is the connection point between the end-effector and the cable. The vector distance is denoted as $\boldsymbol{b}_i$. E_i is the geometric center of the pulley, as shown in Fig. 4(b). The radius of the swivel pulley is r. The unit direction vector of E_iC_i is denoted as $\boldsymbol{u}_{ri}$. The φ_i represents the wrap angle of the swivel pulley. The distance between A_i and E_i is denoted as h. D_i and C_i are the entry and exit points of the cable, respectively. In Fig. 4(c), θ_i denotes the swing angle of the swivel pulley. $\boldsymbol{R}$ is the rotation matrix of the end-effector. For $i = 1, 2, \ldots, m$, there are $2m$ cables in UMCDPR.

The velocity equation for UMCDPR can be directly presented, taking into account the pulley kinematics.

$$\dot{\boldsymbol{l}}_i = \dot{\boldsymbol{p}} + \boldsymbol{\omega} \times \boldsymbol{b}_i + \frac{r\cos\varphi_i - h}{\boldsymbol{y}_{ri} \cdot \boldsymbol{c}_i}(\dot{\boldsymbol{p}} + \boldsymbol{\omega} \times \boldsymbol{b}_i) + \frac{2\cos\varphi_i}{\boldsymbol{y}_{ri} \cdot \boldsymbol{c}_i + h}(\dot{\boldsymbol{p}} + \boldsymbol{\omega} \times \boldsymbol{b}_i) \tag{1}$$

where$\boldsymbol{c}_i = \boldsymbol{p} + \boldsymbol{R} \cdot \boldsymbol{b}_i - \boldsymbol{a}_i$.

The established process of Eq. (1) can be referred to [38] and Appendix A. The relationship between the velocity of the end-effector and the velocities of cables, in consideration of the influence of pulleys on the velocity of the end-effector, is shown by Eq. (1). Furthermore, Eq. (1) can be simplified into

$$k_{pi} = 1 + \frac{r\cos\varphi_i - h}{\boldsymbol{y}_{ri} \cdot \boldsymbol{c}_i} + \frac{2\cos\varphi_i}{\boldsymbol{y}_{ri} \cdot \boldsymbol{c}_i + h} \Rightarrow \dot{\boldsymbol{l}}_i = k_{pi}(\dot{\boldsymbol{p}} + \boldsymbol{\omega} \times \boldsymbol{b}_i) \tag{2}$$

where k_{pi} is constant. Finally, the cable velocity is obtained as

$$\begin{aligned} &\dot{\boldsymbol{l}}_i = k_{pi}(\dot{\boldsymbol{p}} + \boldsymbol{\omega} \times \boldsymbol{b}_i) \Rightarrow \dot{l}_i = k_{pi}\boldsymbol{u}_i^T(\dot{\boldsymbol{p}} + \boldsymbol{\omega} \times \boldsymbol{b}_i) \\ &\Rightarrow \dot{\boldsymbol{L}} = [\dot{l}_1 \quad \dot{l}_2 \quad \cdots \quad \dot{l}_m]^T = k_{pi}\boldsymbol{J}\left[\dot{\boldsymbol{p}}^T, \boldsymbol{\omega}^T\right]^T = k_{pi}\boldsymbol{J}\widetilde{\boldsymbol{E}}\dot{\boldsymbol{\varepsilon}} = k_{pi}\widetilde{\boldsymbol{J}}\dot{\boldsymbol{\varepsilon}} \end{aligned} \tag{3}$$

where $\boldsymbol{u}_i$ is the unit vector of the cable. Utilizing the operational rules of scalar triple product, we have $\boldsymbol{u}^T{}_i(\boldsymbol{\omega} \times \boldsymbol{b}_i) = (\boldsymbol{b}_i \times \boldsymbol{u}_i)^T\boldsymbol{\omega}$. $\boldsymbol{J} = [\boldsymbol{u}_1, \boldsymbol{u}_2, \boldsymbol{u}_3, \boldsymbol{u}_4; \boldsymbol{u}_1 \times \boldsymbol{R}\cdot\boldsymbol{b}_1, \boldsymbol{u}_2 \times \boldsymbol{R}\cdot\boldsymbol{b}_2, \boldsymbol{u}_3 \times \boldsymbol{R}\cdot\boldsymbol{b}_3, \boldsymbol{u}_4 \times \boldsymbol{R}\cdot\boldsymbol{b}_4]$ is force Jacobian matrix, $\widetilde{\boldsymbol{E}} = [\boldsymbol{I}_{3\times3} \quad \boldsymbol{0}_{3\times3}; \quad \boldsymbol{0}_{3\times3} \quad \boldsymbol{E}_{3\times3}]$, $\dot{\boldsymbol{\omega}} = \boldsymbol{E}_{3\times3}\dot{\boldsymbol{\Phi}}$, $\widetilde{\boldsymbol{J}} = \boldsymbol{J}^T\widetilde{\boldsymbol{E}}$. $\boldsymbol{E}_{3\times3}$ is related to the rotation matrix $\boldsymbol{R}$. The matrix $\boldsymbol{R}$ is described by Euler angles. When the kinematics of the pulleys are not considered, the cable velocity in UMCDPR can be expressed as [39]

$$\dot{\boldsymbol{L}} = \widetilde{\boldsymbol{J}}(\boldsymbol{\varepsilon})\dot{\boldsymbol{\varepsilon}} \tag{4}$$

When comparing the differences between Eqs. (3) and (4), Eq. (3) contains an additional term, k_{pi}, which is mathematically more

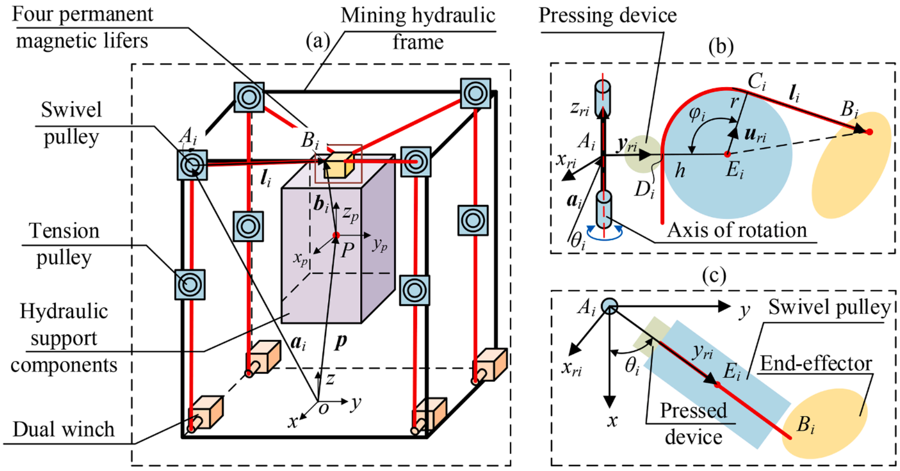

Fig. 4. (a) UMCDPR kinematic model; (b) Side view of the swivel pulley; (c) Top view of the swivel pulley.

complex than Eq. (4). In the harsh underground environment, this significantly escalates the complexity of the control system. Consequently, k_{pi} is approximated to 1 in order to simplify the control system and the static stiffness model. k_{pi} is defined as the correction factor for cable velocity when considering the swivel pulley.

2.4. Task workspace

For this part of the work, the TW of UMCDPR is further optimized to make the distribution of k_{pi} within the TW close to 1. Firstly, considering the varying sizes of the hydraulic support components, it is necessary to leave a certain safety distance within the mining hydraulic frame with 0.5m on both the left and right sides, to prevent the end effector from coming into contact with the mining hydraulic frame; Then, to avoid the situation where the small inclination angle of cables in the horizontal direction fails to counterbalance the gravity of end-effector and to prevent end-effector from touching the bottom of mining hydraulic frame, a space of 1.28m needs to be left in the height direction. Lastly, a space of 1m should be left at the front and back of the mining hydraulic frame to facilitate the work of operators. Thus, the UMCDPR motion region should be smaller than the mining hydraulic frame. Considering the largest possible size of the end-effector, we obtain $||\boldsymbol{b}_i|| = 2.78$ m. The relevant parameters are shown in Table 1. The TW represents the permissible range of motion for point P and the pre-optimized task workspace.

To identify sections within TW where the k_{pi} approximates 1, an initial step involves conducting a sampling analysis of points within the TW, from which it is observed that the maximum k_{pi} is approximately 6.20, 5.80, 6.20, and 5.80, respectively. When k_{pi} is instead ignored, it may result in significant differences between the end-effector and the cable end speed, increasing the risk of safety incidents. The pulley greatly affects the end speed of UMCDPR. The main processing steps and the k_{pi} corresponding to each cable are shown in Table 2.

The final k_{pi} distribution in the TW of UMCDPR is shown in Fig. 5. The distribution of k_{pi} boundary values in TW_t is shown in Table 2. To distinguish between the TW before and after optimization, the optimized TW is defined as TW_t. The trajectories in the following sections are all optimized within TW_t. From the results, the differences in k_{pi} distribution are minimal, so the mean k_{pi} distribution in TW_t can be directly calculated. Since the motion accuracy requirements for the hydraulic support components are not high during the hoisting process of UMCDPR, Eq. (2) can be directly simplified to a constant in the subsequent stiffness model correction process, *i.e.* the mean value of the k_{pi}.

3. Developed ROSD multi-trajectory optimization

This section introduces ROSD and offline multi-trajectory optimization methods. Although we simplify the k_{pi} via optimizing TW, which still impacts the mathematical model of UMCDPR, particularly the static stiffness model. Hence, the static stiffness model of UMCDPR is modified using the simplified k_{pi}. To achieve the task objectives of UMCDPR, ROSD is proposed depending on the modified stiffness model. This index provides a criterion for the offline multi-trajectory in disturbed environments and global visualization to help non-professional users select the best stiffness trajectory. Considering the task objectives, conventional trajectory optimization methods are difficult to apply, leading to the proposal of a new optimization method.

3.1. Correction of UMCDPR static stiffness model

The equilibrium equation of UMCDPR under quasi-static conditions can be expressed as

$$\boldsymbol{J}\boldsymbol{T} + \boldsymbol{W}_e = 0 \tag{5}$$

where UMCDPR cable tension is $\boldsymbol{T} = [t_1,\ t_2,\ t_3,\ t_4]^T$, external force is $\boldsymbol{W}_e = [\boldsymbol{f}_e;\ \boldsymbol{m}_e]^T$. The stiffness equation of UMCDPR can be established as

$$\Delta \boldsymbol{W}_e = \boldsymbol{K}\Delta\boldsymbol{\varepsilon} \tag{6}$$

where $\boldsymbol{K}$ is the stiffness matrix of the system. The expression of the stiffness matrix is derived by taking the derivative of Eq. (6) concerning the general coordinate $\boldsymbol{\varepsilon}$, which can be described as

$$\frac{\partial \boldsymbol{W}_e}{\partial \boldsymbol{\varepsilon}} + \frac{\partial \boldsymbol{J}}{\partial \boldsymbol{\varepsilon}}\boldsymbol{T} + \boldsymbol{J}\frac{\partial \boldsymbol{T}}{\partial \boldsymbol{\varepsilon}} = 0 \quad \Leftrightarrow \quad \frac{\partial \boldsymbol{W}_e}{\partial \boldsymbol{\varepsilon}} = -\frac{\partial \boldsymbol{J}}{\partial \boldsymbol{\varepsilon}}\boldsymbol{T} - \boldsymbol{J}\frac{\partial \boldsymbol{T}}{\partial \boldsymbol{\varepsilon}} = \boldsymbol{K}_1 + \boldsymbol{K}_2 \tag{7}$$

Table 1
UMCDPR structure parameters.

Name	Relevant parameters
The size of the mining hydraulic frame	Length: 30 m, Width: 5 m, Height: 5m
The distance between P and B_i, denoted as $\|\|\boldsymbol{b}_i\|\|$	2.78m
The radius of the pulley size r	0.02m
The turning radius of the pulley h	0.08m
TW	Length: 28 m, Width: 4 m, Height: 2.44m

Table 2
Changes in k_{pi} distribution within TW and processing procedure of k_{pi}.

Steps	The optimization process of k_{pi}	k_{p1}	k_{p2}	k_{p3}	k_{p4}
1	Remove the unreasonable points	6.195~-5.673	5.803~-5.845	6.195~-5.673	5.803~-5.845
	Mean	6.20	5.80	6.20	5.80
2	3 times deviation filter points	1.114~0.649	1.083~0.664	1.114~0.649	1.083~0.664
3	Identify the intersection points and remove discontinuous TWs.	1.079~0.802	1.082~0.664	1.079~0.802	1.082~0.664
	Mean	0.883	0.880	0.883	0.880

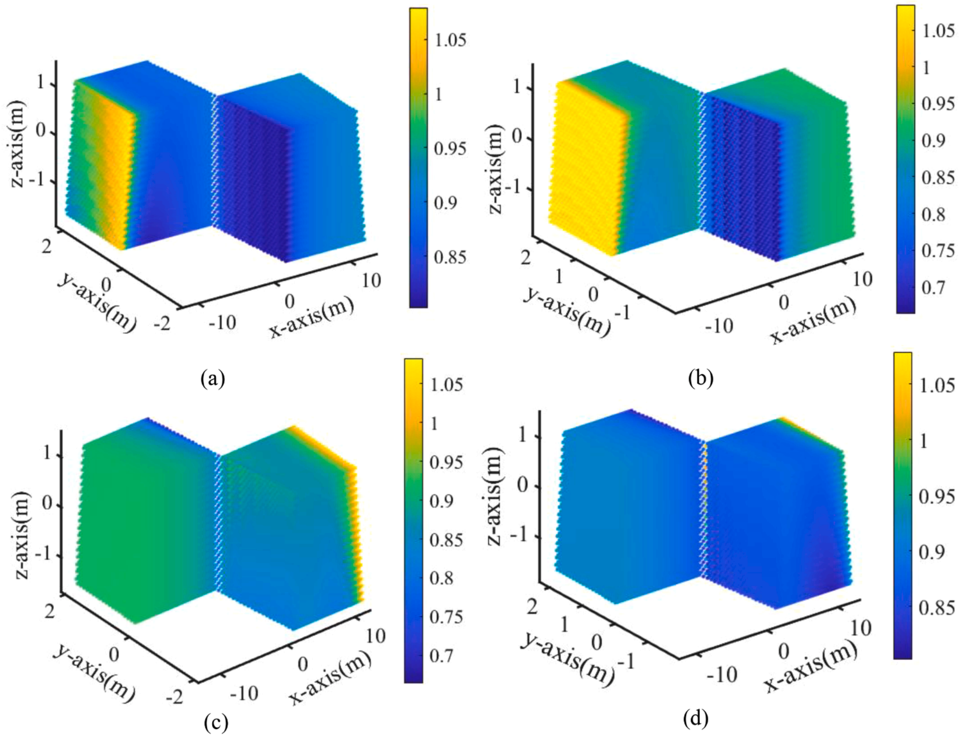

(a) (b) (c) (d)

Fig. 5. (a) The distribution of k_{p1} value in TW_t. (b) The distribution of k_{p2} value in TW_t. (c) The distribution of k_{p3} value in TW_t. (d) The distribution of k_{p4} value in TW_t. The color bar represents the k_{pi} value.

where the stiffness matrix $\boldsymbol{K}$ is divided into two types: one type is the controllable stiffness $\boldsymbol{K}_1$, and the other is the inherent stiffness $\boldsymbol{K}_2$. $\boldsymbol{K}_1$ can be controlled by adjusting the cable tension when the end-effector is at a specific pose. $\boldsymbol{K}_2$ is related to the system structure and the end-effector's pose. In considering the influence of pulley kinematics on the end-effector, the mathematical descriptions for $\boldsymbol{K}_1$ and $\boldsymbol{K}_2$ are no longer applicable. This article corrects some of the formulas presented in [30]. First, Eq. (3) can be further expanded as

$$\begin{aligned}\dot{\boldsymbol{l}}_i &= \dot{l}_i \cdot \boldsymbol{u}_i + l_i \cdot \dot{\boldsymbol{u}}_i = \bar{k}_{pi} \cdot \dot{\boldsymbol{p}} + \bar{k}_{pi} \cdot \dot{\boldsymbol{\omega}} \times \boldsymbol{b}_i \\ &= \bar{k}_{pi}[\boldsymbol{I} \quad -\boldsymbol{b}_i \times \boldsymbol{E}_{3\times 3}]\dot{\boldsymbol{\varepsilon}} = \bar{k}_{pi}\boldsymbol{G}_{pi}\dot{\boldsymbol{\varepsilon}}\end{aligned} \tag{8}$$

where $\boldsymbol{G}_{pi} \in \mathrm{R}^{3\times 6}$ denotes the algebraic matrix, $\bar{k}_{pi}$is the mean value of k_{pi} in TW_t. From Eq. (3), The following is obtained as

$$\dot{l}_i \boldsymbol{u}_i = \boldsymbol{u}_i \bar{k}_{pi}[\widetilde{\boldsymbol{J}}]_i \dot{\boldsymbol{\varepsilon}} \tag{9}$$

where $[\cdot]_i$ is the i-th row of the matrix. Furthermore, Eq. (9) can be simplified as follows:

$$\dot{l}_i \boldsymbol{u}_i = \bar{k}_{pi} \begin{bmatrix} \cos\alpha_i [\widetilde{\boldsymbol{J}}]_i \\ \cos\beta_i [\widetilde{\boldsymbol{J}}]_i \\ \cos\gamma_i [\widetilde{\boldsymbol{J}}]_i \end{bmatrix} \dot{\boldsymbol{\varepsilon}} = \bar{k}_{pi} \boldsymbol{Q}_i \dot{\boldsymbol{\varepsilon}} \tag{10}$$

where $\boldsymbol{u}_i = [\cos\alpha_i \ \cos\beta_i \ \cos\gamma_i]^T$, $\cos^2\alpha_i + \cos^2\beta_i + \cos^2\gamma_i = 1$. Hence, it follows that

$$\frac{\partial \boldsymbol{u}_i}{\partial \boldsymbol{x}_j} = \overline{k}_{pi}\left[\left[-s\alpha_i, 0, \frac{ca_i \cdot sa_i}{c\gamma_i}\right]^T \cdot \frac{\partial \alpha_i}{\partial \varepsilon_j} + \left[0, -s\beta_i, \frac{c\beta_i \cdot s\beta_i}{c\gamma_i}\right]^T \cdot \frac{\partial \alpha_i}{\partial \varepsilon_j}\right] \tag{11}$$

Further, the Hessian matrix can be depicted as

$$\boldsymbol{H}_p^j = \begin{bmatrix} \dfrac{\partial \boldsymbol{u}_1}{\partial \boldsymbol{x}_j} & \cdots & \dfrac{\partial \boldsymbol{u}_m}{\partial \boldsymbol{x}_j} \\ \dfrac{\partial [\boldsymbol{R} \cdot \boldsymbol{b}_i] \times \boldsymbol{u}_1}{\partial \boldsymbol{x}_j} & \cdots & \dfrac{\partial [\boldsymbol{R} \cdot \boldsymbol{b}_m] \times \boldsymbol{u}_m}{\partial \boldsymbol{x}_j} \end{bmatrix} \tag{12}$$

Finally, the controllable stiffness matrix of UMCDPR, taking into account pulley kinematics, is obtained as

$$\boldsymbol{K}_1 = -\boldsymbol{H}_p \boldsymbol{T}, \qquad \boldsymbol{H} = \begin{bmatrix} \boldsymbol{H}_p^1 & \boldsymbol{H}_p^2 & \cdots & \boldsymbol{H}_p^n \end{bmatrix} \in \mathrm{R}^{n \times n \times m} \tag{13}$$

where n represents the DOFs of the end-effector. m is the number of cables.

Considering the pulley kinematics of UMCDPR, the properties of the cables remain unchanged. Therefore, the inherent stiffness $\boldsymbol{K}_2$ can be directly modified as

$$\boldsymbol{K}_2 = \overline{k}_{pi}^2 \widetilde{\boldsymbol{J}} \cdot \mathrm{diag}\left(\frac{E_1 \cdot A_1}{l_{o1}}, \cdots, \frac{E_m \cdot A_m}{l_{om}}\right) \cdot \widetilde{\boldsymbol{J}}^T \tag{14}$$

where E_i, A_i, and l_{oi} are intrinsic properties of the cables. The system stiffness of the modified UMCDPR is

$$\boldsymbol{K}_p = \boldsymbol{K}_1 + \boldsymbol{K}_2 \tag{15}$$

The above are the vital revision formulas for the static stiffness matrix of UMCDPR, which is equally applicable to other CDPRs considering the swivel pulley kinematics. Based on **Assumption 1**, when the position of UMCDPR is determined, $\boldsymbol{K}_2$ cannot be changed. Therefore, this article mainly focuses on analyzing $\boldsymbol{K}_1$. To simplify the subsequent description, the terms "stiffness" and "deformation" mentioned in Sections 3.2 to 4.2 specifically refer to controllable stiffness and controllable deformation.

3.2. Robust optimal stiffness direction

For the first task objective, the index of reflecting stiffness needs to be prevented from failing when UMCDPR is subjected to strong disturbance environments. Generally, stiffness itself functions as a measure of the stability of UMCDPR. When stiffness increases, the robot's ability to resist external disturbances becomes stronger, and the index reflecting stiffness at this time becomes more accurate. In other words, the accuracy of indices reflecting the robot's performance can decrease when disturbances increase, ultimately leading to their failure [13]. The same phenomenon occurs for the index reflecting stiffness. Essentially, by maximizing the stiffness of UMCDPR, the robustness of the index reflecting stiffness at that time is maximized, and the degree of mismatch between offline simulations and actual experiments can be minimized simultaneously.

The length of the semi-axis of the stiffness ellipsoid is related to the magnitude of the eigenvalues of the stiffness matrix, and the direction corresponding to its eigenvectors can be used as a reference direction for trajectory planning [40]. For the second task objective, to associate stiffness with the motion trajectory, the stiffness/compliance ellipsoid index can be used as an inspiration, simultaneously considering the relationship between direction and stiffness. By aligning the eigenvector associated with the eigenvalue of the stiffness matrix, significant stiffness can be achieved in the direction of motion [41]. Based on this, it can be deduced that, when stiffness is maximized, there exists an optimal stiffness direction $\boldsymbol{\tau}_{\min}$. When the motion direction of UMCDPR coincides with or approximates $\boldsymbol{\tau}_{\min}$, it ensures that the stiffness during movement is maximized or approximated for maximization. In this respect, the optimal stiffness direction $\boldsymbol{\tau}_{\min}$ can be found, and UMCDPR can be controlled to always move along this direction. As a result, a trajectory that maximizes the robot's stiffness can be obtained.

Nonetheless, $\boldsymbol{\tau}_{\min}$ is a unit vector that only represents direction, so it cannot assess the magnitude of stiffness. Alternatively, we cannot accurately measure whether this direction is the optimal stiffness direction. Typically, the amount of deformation can serve as a measure of the robot's stiffness, so the relationship of max $\boldsymbol{K}_p \Leftrightarrow$ min $\Delta\boldsymbol{\varepsilon}$ can be established. The magnitude of deformation can be indirectly reflected by the magnitude of the eigenvalue, and the eigenvector corresponding to this eigenvalue represents the deformation caused by the direction of motion of the end-effector at this time [30]. When the eigenvalue at this point corresponds exactly to the minimum deformation, its corresponding eigenvector is $\boldsymbol{\tau}_{\min}$, *i.e.* ROSD. Thus, we can determine whether the current direction of motion is the optimal stiffness direction based on the magnitude of the deformation. Suppose ROSD of all points can be represented in the entire TW_t and ROSD of the next motion point can be required. In this case, the optimal stiffness trajectory can be planned by ROSD. Therefore, a connection between ROSD and minimum deformation needs to be established by the relationship between eigenvalues and eigenvectors. Then, the following theorem needs to be proven.

Theorem 1. $\min \| \Delta\boldsymbol{\varepsilon}_p \| = \| \boldsymbol{W}_e \| \sqrt{\lambda_{\min}}$

Proof: First, the flexibility matrix of UMCDPR can be expressed as

$$\Delta\boldsymbol{\varepsilon}_p = \boldsymbol{C}_p \cdot \boldsymbol{W}_e \tag{16}$$

where $\Delta\boldsymbol{\varepsilon}_p = [\Delta\boldsymbol{p}^T, \Delta\boldsymbol{\Phi}^T]^T$, $\Delta\boldsymbol{p} = [\Delta x, \Delta y, \Delta z]^T$, and $\Delta\boldsymbol{\Phi} = [\Delta\alpha, \Delta\beta, \Delta\gamma]^T$. $\boldsymbol{C}_p = \boldsymbol{K}_p^{-1}$. $\Delta\boldsymbol{p}$ and $\Delta\boldsymbol{\Phi}$ represent the linear displacement and angular displacement deformations of the end-effector, respectively. Expanding Eq. (16), it can be illustrated as

$$\begin{bmatrix} \Delta\boldsymbol{p} \\ \Delta\boldsymbol{\Phi} \end{bmatrix} = \begin{bmatrix} \boldsymbol{C}_{fd} & \boldsymbol{C}_{f\delta} \\ \boldsymbol{C}_{md} & \boldsymbol{C}_{m\delta} \end{bmatrix} \begin{bmatrix} \boldsymbol{f}_e \\ \boldsymbol{m}_e \end{bmatrix} \tag{17}$$

where $\boldsymbol{C}_{fd}$ is the force-linear displacement flexibility matrix, $\boldsymbol{C}_{f\delta}$ is the force-angular displacement flexibility matrix, $\boldsymbol{C}_{md}$ is the moment-linear displacement flexibility matrix, and $\boldsymbol{C}_{m\delta}$ is the moment-angular displacement flexibility matrix. The vector $\boldsymbol{u}_d = [\boldsymbol{e}_d\ \boldsymbol{0}_{3\times1}]$ and $\boldsymbol{u}_\delta = [\boldsymbol{0}_{3\times1}\ \boldsymbol{e}_\delta]$, where $\boldsymbol{e}_d$ and $\boldsymbol{e}_\delta$ are the unit vectors of $\Delta\boldsymbol{p}$ and $\Delta\boldsymbol{\Phi}$, respectively. Multiplying Eq. (17) by $\boldsymbol{u}T\ d$ and $\boldsymbol{u}T\ \delta$ on the left, respectively, can be expressed as

$$\begin{bmatrix} \| \Delta\boldsymbol{p} \| \\ \boldsymbol{0}_{3\times1} \end{bmatrix} = \begin{bmatrix} \boldsymbol{e}_d^T\boldsymbol{C}_{fd} & \boldsymbol{e}_d^T\boldsymbol{C}_{f\delta} \\ \boldsymbol{0}_{3\times3} & \boldsymbol{0}_{3\times3} \end{bmatrix} \begin{bmatrix} \boldsymbol{f}_e \\ \boldsymbol{m}_e \end{bmatrix}, \quad \begin{bmatrix} \boldsymbol{0}_{3\times1} \\ \| \Delta\boldsymbol{\Phi} \| \end{bmatrix} = \begin{bmatrix} \boldsymbol{0}_{3\times3} & \boldsymbol{0}_{3\times3} \\ \boldsymbol{e}_\delta^T\boldsymbol{C}_{md} & \boldsymbol{e}_\delta^T\boldsymbol{C}_{m\delta} \end{bmatrix} \begin{bmatrix} \boldsymbol{f}_e \\ \boldsymbol{m}_e \end{bmatrix} \tag{18}$$

Furthermore, by combining Eq. (16) and converting $\Delta\boldsymbol{\varepsilon}_p$ into scalar form, which can be formulated as

$$\| \Delta\boldsymbol{\varepsilon}_p \| = \sqrt{\boldsymbol{W}_e^T\left(\boldsymbol{u}_x^T\boldsymbol{K}_p^{-1}\right)^T\left(\boldsymbol{u}_x^T\boldsymbol{K}_p^{-1}\right)\boldsymbol{W}_e}, \quad \boldsymbol{u}_x = \{\boldsymbol{u}_d, \quad \boldsymbol{u}_\delta\} \tag{19}$$

Replace Eq. (19) with the quadratic standard form matrix $\boldsymbol{S} = (\boldsymbol{u_x}^T\boldsymbol{K_p}^{-1})^T(\boldsymbol{u_x}^T\boldsymbol{K_p}^{-1})$. According to the Rayleigh theorem, the form of Eq. (19) can be transformed into

$$\mathrm{R}(\boldsymbol{S}, \boldsymbol{W}_e) = \frac{\boldsymbol{W}_e^H\boldsymbol{S}\boldsymbol{W}_e}{\boldsymbol{W}_e^H\boldsymbol{W}_e} = \frac{\| \Delta\boldsymbol{\varepsilon}_p \|^2}{\boldsymbol{W}_e^H\boldsymbol{W}_e} \tag{20}$$

The eigenvector of $\boldsymbol{S}$, which is the critical point of the function $\mathrm{R}(\boldsymbol{S}, \boldsymbol{W}_e)$, is the direction vector of $\boldsymbol{W}_e$. The eigenvalue corresponding to the eigenvector is the value of the function $\mathrm{R}(\boldsymbol{S}, \boldsymbol{W}_e)$ at this critical point. Where the eigenvalues $\lambda_{\max}$ and $\lambda_{\min}$ are the maximum and minimum values of matrix $\boldsymbol{S}$, Eq. (20) can be depicted as

$$\lambda_{\max} = \max_{\|\boldsymbol{W}_e\|\neq0} \frac{\boldsymbol{W}_e^H\boldsymbol{S}\boldsymbol{W}_e}{\boldsymbol{W}_e^H\boldsymbol{W}_e}, \lambda_{\min} = \min_{\|\boldsymbol{W}_e\|\neq0} \frac{\boldsymbol{W}_e^H\boldsymbol{S}\boldsymbol{W}_e}{\boldsymbol{W}_e^H\boldsymbol{W}_e} \tag{21}$$

where $\boldsymbol{W}_e^H\boldsymbol{W}_e = \| \boldsymbol{W}_e \|^2$. Combining with Eq. (20), Eq. (21) can be formulated as

$$\| \boldsymbol{W}_e \| \sqrt{\lambda_{\min}} \leq \| \Delta\boldsymbol{\varepsilon} \| \leq \| \boldsymbol{W}_e \| \sqrt{\lambda_{\max}}, \quad \lambda_{\min} = \left\{\lambda_{p\min}, \lambda_{\Phi\min}\right\}, \quad \lambda_{\max} = \left\{\lambda_{p\max}, \lambda_{\Phi\max}\right\} \tag{22}$$

The $\lambda_{p\min}$, $\lambda_{p\max}$, $\lambda_{\Phi\min}$, and $\lambda_{\Phi\max}$ correspond to the eigenvalue coefficients for the minimum and maximum displacement $\Delta\boldsymbol{p}$, as well as the eigenvalue coefficients for the minimum and maximum rotation $\Delta\boldsymbol{\Phi}$, respectively. According to the inequality in Eq. (22), the min $\Delta\boldsymbol{\varepsilon}_p$ can be expressed as

$$\min\left\|\Delta\boldsymbol{\varepsilon}_p\right\| = \min[\|\Delta\boldsymbol{p}\|, \|\Delta\boldsymbol{\Phi}\|]^T = [\|\boldsymbol{W}_e\|\sqrt{\lambda_{p\min}}, \quad \|\boldsymbol{W}_e\|\sqrt{\lambda_{\Phi\min}}]^T \tag{23}$$

Proof completed. Below is ROSD calculation method in TW_t as follows:

```
Method 1:ROSD calculation method in $\mathrm{TW}_t$
Initialization:
  ·$\boldsymbol{p}_j$ is a certain point in $\mathrm{TW}_t$
  ·$\boldsymbol{T}_{max}$, $\boldsymbol{T}_{min}$
  ·$\boldsymbol{W}_e$
  The number of points in $\mathrm{TW}_t$ is $n_t$.
Output:$\boldsymbol{\tau}_{p,j,min}$, $\boldsymbol{\tau}_{\Phi,j,min}$
for $j \leftarrow 1: n_t$ do
    if $\boldsymbol{p}_j \in \mathrm{TW}_t$
        for $\boldsymbol{N}\xi \leftarrow \boldsymbol{T}_{min} + \boldsymbol{J}_i^{\dagger}\boldsymbol{W}_e$: $\boldsymbol{T}_{max} + \boldsymbol{J}_i^{\dagger}\boldsymbol{W}_e$ do Search for $\boldsymbol{T}$ in WFW
            Using Eqs. (13) and (14), to obtain $\boldsymbol{K}_p$, and $\boldsymbol{C}\ p = (\boldsymbol{K}\ p)^{-1}$
            Using Eq. (31), to obtain $\Delta\boldsymbol{\varepsilon}$, determining $\boldsymbol{u}\ xi$
            $\boldsymbol{S}_i = (\boldsymbol{u}T\ xi\boldsymbol{C}\ p)^T\ (\boldsymbol{u}T\ xi\boldsymbol{C}\ p)$
            Solve for eigenvalues $\lambda_{p,i}$ and $\lambda_{\Phi,i}$ of $\boldsymbol{S}_i$, as well as the corresponding eigenvectors $\boldsymbol{\tau}_{p,i}$ and $\boldsymbol{\tau}_{\Phi,i}$.
            Save $\lambda_{p,i}$, $\boldsymbol{\tau}_{p,i}$ in $\boldsymbol{\Omega}_p$, and $\lambda_{\Phi,i}$, $\boldsymbol{\tau}_{\Phi,i}$ in $\boldsymbol{\Omega}_r$, respectively.
        end for
    end if
    min($\boldsymbol{\Omega}_p$)$\rightarrow\lambda_{pmin}$, $\boldsymbol{\tau}_{p,j,min}$ and min($\boldsymbol{\Omega}_r$) $\rightarrow\lambda_{\Phi min}$, $\boldsymbol{\tau}_{\Phi,j,min}$
    $\boldsymbol{\Omega}_p = \emptyset$, $\boldsymbol{\Omega}_r = \emptyset$
end for
```

The stiffness matrix $\boldsymbol{K}_p$ of UMCDPR is determined by the position $\boldsymbol{p}$, orientation $\boldsymbol{\Phi}$, and tension $\boldsymbol{T}$ of the end-effector. The $\boldsymbol{p}$ and $\boldsymbol{\Phi}$

are connected with the position of the end-effector at a certain point in TW$_t$. (based on **Assumption 1,** $\mathbf{\Phi} = \mathbf{0}$). The $\boldsymbol{K}_1$ can be altered by adjusting the tension $\boldsymbol{T}$ at the current pose. From Eq. (5), the force $\boldsymbol{T}$ can be resolved by calculating the Moore–Penrose generalized inverse matrix [42]:

$$\boldsymbol{T} = -\boldsymbol{J}^{\dagger}\boldsymbol{W}_e + \boldsymbol{N}\xi \tag{24}$$

where $\boldsymbol{J}^{\dagger} = \boldsymbol{J}^T(\boldsymbol{J}\boldsymbol{J}^T)^{-1} \in \mathrm{R}^{m\times n}$, $\xi \in \mathrm{R}^r$ is an arbitrary constant, $\boldsymbol{N} \in \mathrm{R}^{m\times r}$ is the null space matrix of $\boldsymbol{J}$, using an m-cable n-DOF CDPR, $r = m - n$. It is necessary to ensure that the cable's tension satisfies condition:$\boldsymbol{T}_{\min} \preceq \boldsymbol{T} \preceq \boldsymbol{T}_{\max}$,$\mathbf{0} \preceq \boldsymbol{T}_{\min} \preceq \boldsymbol{T}_{\max}$. This maximum tension can be related to the torque limits of the motor reeling in the cable or the maximum tension that the cable can withstand without breaking. The minimum tension is to prevent "virtual driven" in the cables during the movement of UMCDPR. Eq. (24) can be formulated as

$$\left\{\xi | \boldsymbol{T}_{\min} + \boldsymbol{J}^{\dagger}\boldsymbol{W}_e \preceq \boldsymbol{N}\xi \preceq \boldsymbol{T}_{\max} + \boldsymbol{J}^{\dagger}\boldsymbol{W}_e\right\} \tag{25}$$

From UMCDPR kinematic, $m = 4$, $n = 3$, $r = 1$, $\xi \in \mathrm{R}$ is one-dimensional, making WFW relatively simple [43]. Since $\boldsymbol{K}_1$ is controllable, the tension $\boldsymbol{T}$ can be adjusted to maximize the stiffness $\boldsymbol{K}_p$ of UMCDPR, which correspondingly reduces $\lambda_{p\min}$. From the above analysis, this ROSD calculation method based on TW$_t$ can be derived *i.e.* **Method 1**. The logic of **Method 1** is as follows: 1) UMCDPR stops at a certain point in TW$_t$ to ascertain WFW. 2) In WFW, ξ is adjusted with a certain step to establish the cable tension $\boldsymbol{T}$, which defines the stiffness matrix $\boldsymbol{K}_p$. 3) The matrix $\boldsymbol{S}$ is obtained according to Eq. (19). 4) The minimum deformation $\boldsymbol{\tau}_{\min}$ at each point in TW$_t$ is confirmed.

3.3. ROSD multi-trajectory optimization method in TW$_t$

As mentioned in Section 3.2, each position point in TW$_t$ contains ROSD. In this section, we need to standardize the movement trajectory of UMCDPR. When the maximum stiffness for each point in TW$_t$ is decided, the direction of $\boldsymbol{\tau}_{\min}$ is also confirmed. At this point, the ROSD distribution within TW$_t$ can be fully observed (Fig. 9). However, for the second task objective, it is difficult to optimal due to the lack of fixed initial and terminal points. Moreover, if UMCDPR consistently moves along the path defined by ROSD, it becomes challenging to fulfill the comprehensive tasks. Therefore, we can effectively segment TW$_t$ and extract the set of points that all possible trajectories of UMCDPR must pass through *i.e.* z-axis. Then, by approximating the motion direction of each sampling point along the trajectory to ROSD, the overall deformation of the trajectory is minimized, and the stiffness $\boldsymbol{K}_p$ is maximized. Finally, the optimal stiffness trajectory can be required.

All sampling points in TW$_t$ satisfy the equation $\boldsymbol{\tau}_{j,\ \min} = \boldsymbol{\tau}_{p,j,\min}$. Assuming the end-effector moves from the initial point $\boldsymbol{p}_0$ to the terminal point $\boldsymbol{p}_n$ along a predetermined trajectory $\mathscr{P}$ in TW$_t$, $t_{j+1} = t_j + \Delta t$. When UMCDPR is located at a point in TW$_t$, its position is $\boldsymbol{p}_j = [x_j, y_j, z_j]^T$, and when it transitions to the next point, the position of UMCDPR is $\boldsymbol{p}_{j+1}$. $\boldsymbol{a}_j$ is the motion direction of UMCDPR at sampling point $\boldsymbol{p}_j$. Δt is the time taken to move from $\boldsymbol{p}_j$ to $\boldsymbol{p}_{j+1}$, representing the unit time step. Discretize the trajectory $\mathscr{P}$ into j path points and describe it in matrix form:

$$\mathbf{P} = [\boldsymbol{p}_0 \ \cdots \ \boldsymbol{p}_j \ \cdots \ \boldsymbol{p}_{n_j}]^T \tag{26}$$

where $P \in \mathrm{R}^{3\times j}$ represents the position trajectory matrix of UMCDPR. Setting a constant speed $\| \dot{\boldsymbol{p}}_j \|$ for the sampling points between $\boldsymbol{p}_j$ and $\boldsymbol{p}_{j+1}$ can be expressed as

$$\| \Delta \boldsymbol{p}_j \| = \| \boldsymbol{p}_{j+1} - \boldsymbol{p}_j \| = \| \dot{\boldsymbol{p}}_j \| \Delta t \qquad 0 \le j \le n-1, j \in \mathbb{N}^+ \tag{27}$$

According to Eq. (27), the motion direction $\boldsymbol{a}_j$ of UMCDPR can be decided as

$$\boldsymbol{a}_j = \frac{\boldsymbol{p}_{j+1} - \boldsymbol{p}_j}{\| \dot{\boldsymbol{p}}_j \| \Delta t} \tag{28}$$

When $\boldsymbol{a}_j$ approaches $\boldsymbol{\tau}_{j,\ \min}$ as closely as possible, the stiffness of UMCDPR at this position becomes closer to the optimal stiffness. Since UMCDPR operates consistently at low speeds, the speed is set to a constant value. This means that the distance traveled during each sampling interval is equal. Likewise, TW$_t$ can be re-divided to ensure that the distance from a sampling point to its surrounding points is $\| \dot{\boldsymbol{p}}_j \| \Delta t$.

3.3.1. TW$_t$ segmentation principle based on Kepler conjecture

Definition 1. The $\boldsymbol{p}_j$ in TW$_t$ has a neighborhood δ, within which the $\boldsymbol{\tau}_{j,min}$ at the point $\boldsymbol{p}_j$ is completely identical. The surrounding neighborhood is called the **unit sphere**, whose position center of the sphere is $\boldsymbol{p}_j$.

Following Definition 1, the existence of both unit spheres can be assumed, with their center located at $\boldsymbol{p}_j$ and $\boldsymbol{p}_{j+1}$ respectively, and both unit spheres have a radius of δ. When UMCDPR moves from $\boldsymbol{p}_j$ to $\boldsymbol{p}_{j+1}$, we have $\delta = \| \dot{\boldsymbol{p}}_j \| \cdot \Delta t / 2$. It is not feasible to divide TW$_t$ into an endless number of points under the real operating conditions of UMCDPR. Generally, the number of sampling points in TW$_t$ is ascertained by δ. Therefore, TW$_t$ can be divided into countless unit spheres with a radius δ, where the center position of each unit sphere is at $\boldsymbol{p}_j$. Meanwhile, the double unit spheres centered at $\boldsymbol{p}_j$ and $\boldsymbol{p}_{j+1}$ are positioned tangentially. δ determines the number of points in TW$_t$. The smaller δ is, the more points there are in TW$_t$, resulting in higher accuracy of the obtained trajectory. The precision of the final trajectory depends on the extent to which the unit spheres cover TW_t. The broader the coverage of the sphere domains over TW_t, the higher the precision of the fitted trajectory, but the greater the burden on the computer. The accuracy of the final result depends on the number of unit spheres in TW_t, but it also places a greater burden on the computer.

Theorem 2. No packing of congruent balls in Euclidean three-space has a density greater than that of the face-centered cubic packing [44,45].

Based on Theorem 2, the TW_t can be divided such that the sampling points are equidistant from their surrounding points, while still ensuring that the optimized trajectory maintains a certain level of accuracy. Theorem 2 is the fundamental principle of Kepler's conjecture, which introduces the concept of face-centered cubic packing and body-centered cubic packing. Meanwhile, the body-centered cubic packing is segmented into quasi-cuboid, which is defined as the segmentation units. This unit is formed by combining one hemisphere and four octant-spheres and comprises five sampling points: four vertices and one center point. This approximation achieves an efficiency of about 74.04 %.

The segmentation schematic is illustrated in Fig. 6(a). TW_t is uniformly divided into unit spheres, where the Euclidean distance between any sampling point $\boldsymbol{p}_j$ and its surrounding point $\boldsymbol{p}_{j+1}$ within TW_t is equal. Additionally, each unit sphere is ensured to be tangent to 12 surrounding unit spheres.

Furthermore, the TW_t segmentation principle is as follows: 1) In the body-centered cubic packing, which is divided into three layers, let's designate the spheres in the middle layer as A (blue) and the spheres in the upper and lower layers as B (green), as show in Fig. 6(a). Here, a form consisting of one sphere A and four spheres B can be regarded as a basic unit of the body-centered cubic packing. This form can be defined as A+4B, as illustrated in Fig. 6(b); 2) When exacting the A+4B structure, there are three ways to divide it, ultimately resulting in a quasi-cuboid, as shown in Fig. 6(c); 3) The quasi-cuboid is composed of four octant-spheres and one hemisphere; 4) Using a quasi-cuboid to fill in the TW_t. Align the four vertices of the quasi-cuboid with the boundaries of TW_t. Arrange the quasi-cuboids sequentially along the *x, y*, and *z* directions of TW_t. In this respect, octant-spheres are stitched along the x-axis or y-axis, whereas hemispheres are stitched along the z-axis. The fill process continues until one of the four vertices extends beyond the boundaries of TW_t. At this point, it can be observed that TW_t fills the unit sphere, with each unit sphere's center representing a sampling point. The flowchart of Kepler's Conjecture segmentation method is shown in Fig. 7. x_d, y_d, and z_d are the lower boundaries of TW_t. Meanwhile, x_u, y_u, and z_u represent the upper boundaries of TW_t. The final output is the segmented TW_t.

Based on the characteristics of the TW_t, it is mainly divided into two parts: one where $x > 0$ and $y < 0$, and the other where $x < 0$ and $y > 0$. The two regions are connected along the z-axis. According to the second task objective, UMCDPR always passes through the z-axis during operation. According to the second task objective, when the UMCDPR moves within the TW_t, it inevitably crosses the z-axis. When initiating the optimization process, it is reasonable to start the search from points located on the z-axis as initial search points. After dividing TW_t using Theorem 2, all the division points on the z-axis are sequentially selected as the multi-initial search points for optimization (note that these initial points for optimization are not the same as the initial points for UMCDPR trajectory). Another benefit of this approach is that it helps prevent the final multi-trajectory optimization from getting trapped in a local optimum and failing to connect the two regions, as illustrated in Fig. 8(a).

3.3.2. *Similarity calculation mechanism*

After segmentation and calculation using **Method 1**, each sampling point in TW_t contains two types of information: positional information $\boldsymbol{p}_j$ and ROSD information $\boldsymbol{\tau}_{j,\min}$. To maximize the stiffness at each point along the UMCDPR trajectory, the similarity between the motion direction $\boldsymbol{a}_j$ and both $\boldsymbol{\tau}_{j,\min}$, and $\boldsymbol{\tau}_{j+1,\min}$ can be formulated as

$$\max\sum_{j=1}^{n_j} S_j\left(\boldsymbol{a}_j,\quad \boldsymbol{\tau}_{j,\min},\quad \boldsymbol{\tau}_{j+1,\min}\right) \Rightarrow \sum_{j=1}^{n_j}\max S_j,\quad \boldsymbol{p}_j \in TW_t \tag{29}$$

where $S_j(\boldsymbol{a}_j, \boldsymbol{\tau}_{j,\min}, \boldsymbol{\tau}_{j+1,\min})$ represents the similarity between $\boldsymbol{a}_j$ and both $\boldsymbol{\tau}_{j,\min}$ and $\boldsymbol{\tau}_{j+1,\min}$. Essentially, when the motion direction $\boldsymbol{a}_j$ is most similar to $\boldsymbol{\tau}_{j,\min}$ and $\boldsymbol{\tau}_{j+1,\min}$, the stiffness of this direction is maximized. The stiffness of each direction on the trajectory P is maximum, and the stiffness of the entire trajectory is also maximum. Since the trajectory is discrete, maximizing the similarity at each step is equivalent to maximizing the overall similarity along the entire trajectory P. Furthermore, the similarity obtained at each step of UMCDPR can be described as

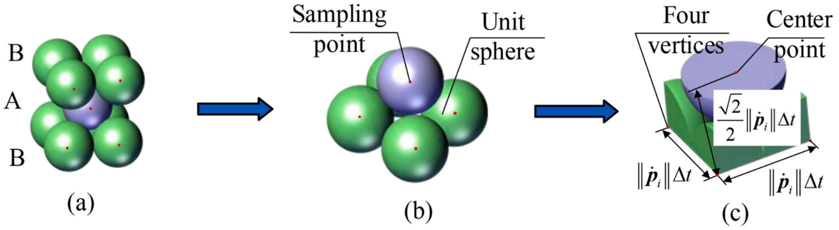

Fig. 6. Mechanism of segmentation TW_t based on Kepler's Conjecture. (a) The body-centered cubic packing; (b) A+4B; (c) Quasi-cuboid.

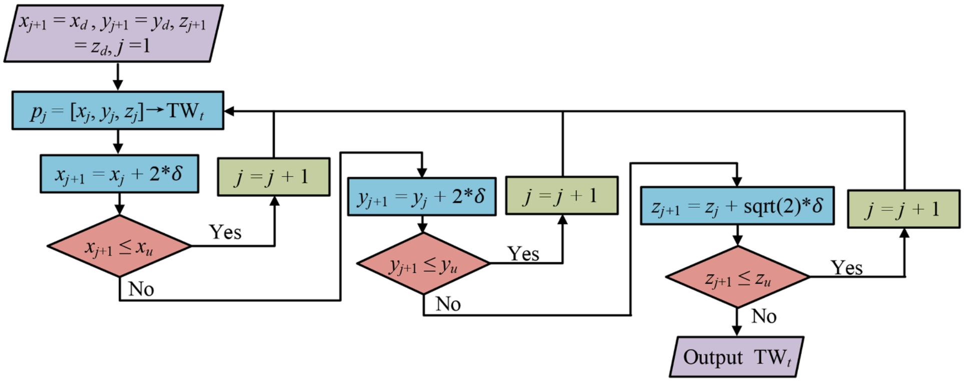

Fig. 7. Flowchart of Kepler's Conjecture segmentation method.

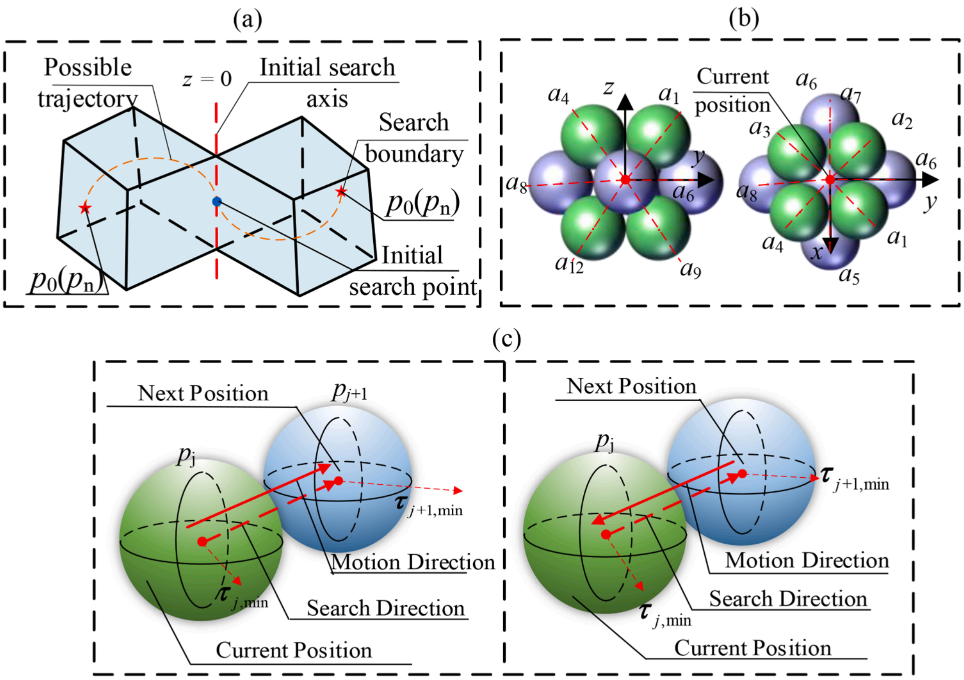

Fig. 8. (a) Initial point selection and search boundaries; (b) Search and motion direction space; (c) Similarity calculation mechanism.

$$S_j = \frac{\boldsymbol{\tau}^T_{j,\min}\left(\boldsymbol{p}_{j+1} - \boldsymbol{p}_j\right)}{\| \dot{\boldsymbol{p}}_j \| \Delta t} + \frac{\boldsymbol{\tau}^T_{j+1,\min}\left(\boldsymbol{p}_{j+1} - \boldsymbol{p}_j\right)}{\| \dot{\boldsymbol{p}}_j \| \Delta t} = \left(\boldsymbol{\tau}_{j,\min} + \boldsymbol{\tau}_{j+1,\min}\right)^T \boldsymbol{a}_j \quad S_j \in [-2, 2] \tag{30}$$

3.3.3. Search and motion direction space

According to the geometric properties of body-centered cubic close packing, each unit sphere is surrounded by 12 neighboring unit spheres. Consequently, when the point $\boldsymbol{p}_j$ moves to $\boldsymbol{p}_{j+1}$ along the P, there are 12 different options available. Each choice of $\boldsymbol{p}_{j+1}$ corresponds to a specific motion direction $\boldsymbol{a}_j$. The current position of the body-centered cubic packing can be set as the origin, with arrangements of $\boldsymbol{a}_1$, $\boldsymbol{a}_2$, …, and $\boldsymbol{a}_{12}$ exhibiting symmetry and uniformity. The arrangement directions of $\boldsymbol{a}_1 \sim \boldsymbol{a}_4$ represent the edges of a regular tetra pyramid, with the sphere's center as the apex. The directions of $\boldsymbol{a}_9 \sim \boldsymbol{a}_{12}$ correspond to four symmetric edges formed by reflecting $\boldsymbol{a}_1 \sim \boldsymbol{a}_4$ across the *xoy* plane. Meanwhile, the arrangement of $\boldsymbol{a}_5 \sim \boldsymbol{a}_8$ forms a cross shape with the unit sphere at $\boldsymbol{p}_j$ as its center, as shown in Fig. 8(b).

Based on the geometric relationships of $\boldsymbol{a}_1 \sim \boldsymbol{a}_{12}$, the unit vector coordinates for each can be expressed as follows: $\boldsymbol{a}_1 = [0.5, 0.5, 0.707]^T$, $\boldsymbol{a}_2 = [-0.5, 0.5, 0.707]^T$, $\boldsymbol{a}_3 = [-0.5, -0.5, 0.707]^T$, $\boldsymbol{a}_4 = [0.5, -0.5, 0.707]^T$, $\boldsymbol{a}_5 = [1, 0, 0]^T$, $\boldsymbol{a}_6 = [0, 1, 0]^T$, $\boldsymbol{a}_7 = [-1, 0, 0]^T$, $\boldsymbol{a}_8 = [0, -1, 0]^T$, $\boldsymbol{a}_9 = [0.5, 0.5, -0.707]^T$, $\boldsymbol{a}_{10} = [-0.5, 0.5, -0.707]^T$, $\boldsymbol{a}_{11} = [-0.5, -0.5, -0.707]^T$, $\boldsymbol{a}_{12} = [0.5, -0.5, -0.707]^T$. Based on the characteristics of TW_t, when selecting a point on the z-axis as the starting point for an outward search, there are two possible search directions along the x-axis. The search direction is continually ensured to form an acute angle with the x-axis to prevent repeat searches at the same position. Generally, the search directions are divided into two groups: one group coincides with the motion direction and another opposes it. The forward or backward of the search direction depends on reaching the TW_t boundary as the trajectory's terminal or initial point, as shown in Fig. 8(c). This results in two distinct search direction $\boldsymbol{a}_j$ spaces:

$$\begin{cases} \mathbf{A}_{x+} = \{\boldsymbol{a}_1 \quad \boldsymbol{a}_4 \quad \boldsymbol{a}_5 \quad \boldsymbol{a}_6 \quad \boldsymbol{a}_8 \quad \boldsymbol{a}_9 \quad \boldsymbol{a}_{12}\} \\ \mathbf{A}_{x-} = \{\boldsymbol{a}_2 \quad \boldsymbol{a}_3 \quad \boldsymbol{a}_6 \quad \boldsymbol{a}_7 \quad \boldsymbol{a}_8 \quad \boldsymbol{a}_{10} \quad \boldsymbol{a}_{11}\} \end{cases} \tag{31}$$

where each direction space contains seven directions, with the two sets of directions contrasting to each other. In $\mathbf{A}_{x+}$, the search direction corresponds with the motion direction, while in $\mathbf{A}_{x-}$, the search direction opposes the motion direction. This setup facilitates subsequent multi-trajectory optimization.

The calculation method for ROSD offline multi-trajectory optimization in TW_t is as follows:

```
Method 2: ROSD offline multi-trajectory optimization method in $\mathrm{TW}_t$.
Initialization:
  ·$\mathrm{TW}_t$
  ·Unit sphere radius $\delta$.
Output: The trajectory $P$
Based on the face-centered cubic close packing, $\mathrm{TW}_t$ is segmented to generate a series of points $\boldsymbol{p}_j$.
for $i = 1, M$ do There are $M$ initial points on the z-axis.
  while $\boldsymbol{p}_{j+1} \in \mathrm{TW}_t$ do
    for $n = 1, 7$ do Iterate through all $\boldsymbol{a}_n$ within the motion direction space.
      if $\boldsymbol{p}_j \in \{(x,y) | x>0, y<0\}$
        $\boldsymbol{a}_n \leftarrow \mathbf{A}_{x+}$
      else
        $\boldsymbol{a}_n \leftarrow \mathbf{A}_{x-}$
      end if
      Using $\boldsymbol{p}_{j+1} = \boldsymbol{p}_j + 2\delta \cdot \boldsymbol{a}_n$, Method 1$(\boldsymbol{p}_{j+1}, \boldsymbol{p}_j) \rightarrow \boldsymbol{\tau}_{j+1,\min}, \boldsymbol{\tau}_{j,\min}$.
      Using Eq. (30), obtain $S_j$, and save $S_j$ in $\boldsymbol{S}$.
    end for
    $S_{max} = \max(\boldsymbol{S})$
    Record the $\boldsymbol{p}_{j+1}$ corresponding to the maximum value $S_{max}$, $P \leftarrow p_{j+1}$
  end while
end for
```

In summary, the flow of ROSD offline multi-trajectory optimization in TW_t is as follows:

(1) By setting an appropriate δ, TW_t can be divided into a finite number of unit spheres following the principle of Kepler's conjecture segmentation. Based on the distribution rules of ROSD, the two assembling areas are determined to be either the initial area or the final assembly area, with this determination being discussed further in Section 4.1;

(2) After completing the segmentation of TW_t, an initial point is selected on the z-axis to commence the search. Depending on the terminal or initial areas of the trajectory, a decision is made regarding whether $\boldsymbol{p}_{j+1}$ should choose the search space of $\mathbf{A}_{x+}$ or $\mathbf{A}_{x-}$ at this point. Meanwhile, search boundaries and initial points are determined by the characteristics of TW_t and the task objectives of UMCDPR;

(3) From the search and motion direction space, select $\boldsymbol{a}_j$ to decide $\boldsymbol{p}_{j+1}$. Utilize **Method 1** to ascertain $\boldsymbol{\tau}_{j+1,\min}$ and $\boldsymbol{\tau}_{j,\min}$, and subsequently calculate the similarity value between $\boldsymbol{a}_j$ and both $\boldsymbol{\tau}_{j+1,\min}$ and $\boldsymbol{\tau}_{j,\min}$ as indicated by the similarity calculation mechanism;

(4) After iterating through all possible $\boldsymbol{a}_j$, select the $\boldsymbol{p}_{j+1}$ corresponding to the maximum similarity value. This calculation process is repeated until $\boldsymbol{p}_{j+1}$ exceeds the boundary of TW_t.

Finally, the flowchart of the ROSD offline multi-trajectory optimization method in TW_t is obtained. Since this method selects multiple sets of initial points from the z-axis to form multiple trajectories and ultimately selects the trajectory with the optimal stiffness, it is called the "multi-trajectory optimization method."

4. Numerical simulations

This section intends to validate the vital conclusions from the previous sections through two groups of numerical simulations. Eventually, the trajectory with the minimal maximum deformation of 0.027 m is selected as the motion trajectory of UMCDPR. These two numerical simulations validate the properties of ROSD and achieve both task objectives. The conclusions are as follows: 1) When the mean value of disturbances falls within the disturbance capacity, the ROSD in this state can serve as an index for offline optimization of the UMCDPR; 2) An optimal stiffness trajectory is obtained based on the distribution rule of ROSD. Upon verification, the maximum displacement along this trajectory falls within the safe distance range.

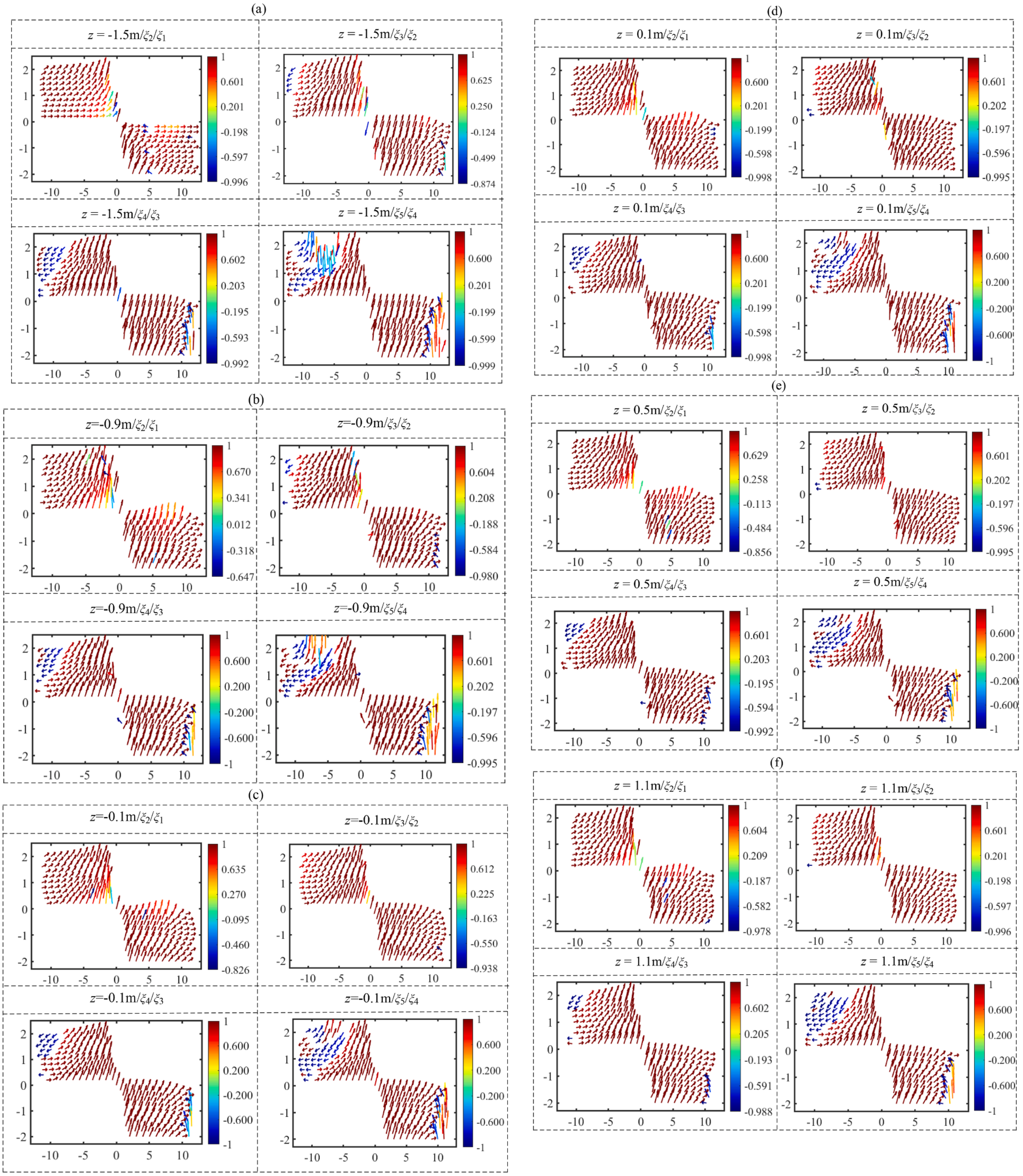

Fig. 9. Experimental results of ROSD robustness verification. (a) The distribution of ROSD in the plane where z = -1.5. (b) The distribution of ROSD in the plane where z = -0.9. (c) The distribution of ROSD in the plane where z = -0.1. (d) The distribution of ROSD in the plane where z = 0.1. (e) The distribution of ROSD in the plane where z = 0.5. (f) The distribution of ROSD in the plane where z = 1.1.

4.1. ROSD robustness verification

Firstly, to achieve the two task objectives, we need to verify whether ROSD can maintain a consistent distribution rule when the disturbance is within a certain range, thereby ensuring that the offline simulation results are more reliable for underground experiments. Five sets of numerical simulations and four comparison results are designed to evaluate the robustness of ROSD. Based on Table 1, we have supplemented the relevant parameters.

4.1.1. Simulation steps

1. Based on **Assumption 1**, UMCDPR has 3-DOF translation. Considering the gravity acting on the end-effector, the magnitude of the external force is selected as $\boldsymbol{W}_e = [0, 0, -mg]^T$;
2. Partition the TW_t into six distinct planes: $z = 1.1$ m, $z = 0.5$ m, $z = 0.1$ m, $z =$ -0.1 m, $z =$ -0.9 m, and $z =$ -1.5 m, and analyze the variations exhibited by ROSD on each of these partitioned planes;
3. A disturbance ξ_i is introduced to the external force. We have $\boldsymbol{W}_e = [\xi_i, \xi_i, -mg+\xi_i]^T$. The simulation is divided into five groups, with different mean values for ξ_i: $\xi_1 = 0$, $\xi_2 = 50 + \text{sqrt}(0.01)*randn$, $\xi_3 = 500 + \text{sqrt}(0.01)*randn$, $\xi_4 = 1000 + \text{sqrt}(0.01)*randn$, $\xi_5 = 2000 + \text{sqrt}(0.01)*randn$. The function *randn* in MATLAB returns a random scalar drawn from a standard normal distribution. Meanwhile, we select $\delta = 0.4$ to sample points in TW_t, generating ROSD projection onto the *xoy* plane;
4. The cosine similarity is chosen to evaluate ROSD changes as the disturbance progresses from ξ_i to ξ_{i+1}. The similarity formula can be formulated as

$$S = \frac{\boldsymbol{\tau}_{\delta i} \cdot \boldsymbol{\tau}_{\delta i+1}}{\| \boldsymbol{\tau}_{\delta i} \| \| \boldsymbol{\tau}_{\delta i+1} \|} \tag{32}$$

where $\boldsymbol{\tau}_{\delta i}$ and $\boldsymbol{\tau}_{\delta i+1}$ represent ROSD under different disturbances, with $S \in [-1, 1]$. The closer S is to 1, the higher the similarity value between ROSD before and after the disturbance, indicating greater robustness of ROSD at that point. Ultimately, the initial areas and terminal areas are determined based on the distribution pattern of ROSD.

4.1.2. Simulation results

The simulation results are shown in Fig. 9(a) to (f). Meanwhile, Sum the x-axis coordinate values of ROSD and plot a bar chart based on the y-axis and z-axis coordinates of ROSD, as shown in Fig. 10(a) to (f), leading to two results:

1. **ROSD robustness results:** Fig. 9 can be regarded as illustrating the distribution rule of ROSD in TW_t under different disturbances. The horizontal axis represents the x-axis of the TW_t, and the vertical axis represents the y-axis of the TW_t. This figure depicts the distribution rule of ROSD in the three-dimensional workspace by establishing six planes with the z-axis as the normal vector at the levels of $z =$ -1.5 m, $z =$ -0.9 m, $z =$ -0.1 m, $z = 0.1$ m, $z = 0.5$ m, and $z = 1.1$ m to slice the TW_t. (Since it is difficult to observe the distribution rule of ROSD in the three-dimensional space of TW_t, we choose to project ROSD onto different planes. Furthermore, given the task objectives of this article, which involves transporting the mobile load from the negative x-half axis to the positive x-half axis, we select planes parallel to the xoy plane for projection.). Fig. 9 represents the distribution of ROSD after it has been projected onto six planes under different disturbances. Since ROSD merely represents the desired motion direction of the end-effector at each point in TW_t, it is represented by arrows. A general representation for a title is defined as $z = a/\xi_i/\xi_{i+1}$. The title "$z = a$" indicates that the coordinate of this plane is a. The first ξ_i indicates the current disturbance mean for UMCDPR, while the second ξ_{i+1} refers to the disturbance mean being compared. For example, "$z =$ -1.5m/ξ_2/ξ_1" represents ROSD distribution on the $z =$ -1.5 m plane under disturbance ξ_2, with the color bar showing the similarity values when compared to ROSD under disturbance ξ_1. When the disturbance shifts from ξ_i to ξ_{i+1}, the areas with the greatest changes in similarity appear firstly at the boundaries of the TW_t. This denotes that UMCDPR is highly prone to instability when moving the boundaries of TW_t. In most areas, the colors are almost entirely dark red, indicating that the similarity value of ROSD remains consistently close to 1 when the disturbance varies from ξ_i to ξ_{i+1}. Especially when the disturbances from ξ_3 change to ξ_1, the area of dark red is the largest of the comparing results. However, as the ξ_i increases, the areas with notable ROSD changes expand further into the interior of the TW_t. These areas, shown in blue, suggest lower similarity values and that ROSD experiences greater directional shifts under larger disturbances;
2. **ROSD along the x-axis distribution rule:** When the disturbance mean value does not exceed ξ_3, the sum components of the ROSD along the x-axis (*i.e.* the x-coordinates cumulative sum of the ROSD) $>>$ 0, maintaining a level around 50. This indicates that, on the whole, the directional component of the ROSD along the x-axis is consistent with the direction of the x-axis (Fig. 10(a) and Fig. 10(b)). However, when the disturbance mean value exceeds ξ_3, the sum of the components of the ROSD along the x-axis can be less than 0 (Fig. 10(d) and Fig. 10(e)). This also suggests that the disturbance capacity of the ROSD does not exceed ξ_3. Secondly, in Fig. 10(c), the sum of the components of the ROSD along the x-axis is less than 0, and this phenomenon starts from the edge of the TW_t (where $y = 0$ represents the boundary value of the TW_t). These two results are consistent with the variation rule of the ROSD disturbance shown in Fig. 9.

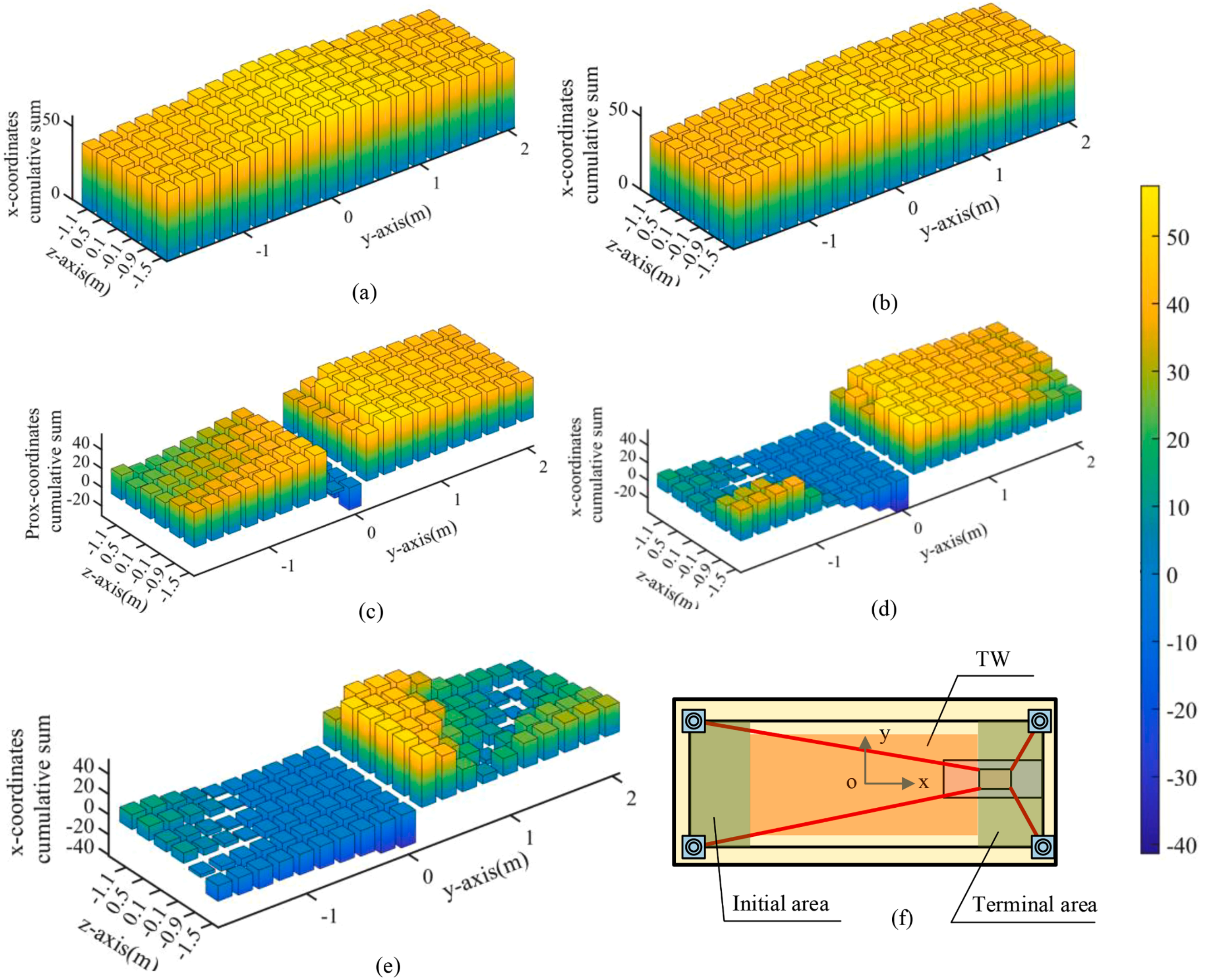

Fig. 10. The sum of the x-coordinate values of ROSD under different disturbances. (a) When the disturbance is ξ_1;(b) When the disturbance is ξ_2; (c) When the disturbance is ξ_3; (d) When the disturbance is ξ_4; (e) When the disturbance is ξ_5. "x-coordinates cumulative sum" represents the cumulative sum of the x-coordinate values of ROSD. "z-axis" represents the z-coordinate of ROSD. "y-axis" represents the y-coordinate of ROSD.

4.1.3. Discussion and analysis

When the mean value of the disturbance affecting ROSD is within a certain range, there always are some areas with a similarity value of 1. These areas are defined as "insensitive areas." The disturbance capacity is the critical disturbance, which suggests that it can trigger changes in insensitive areas. In other words, When the disturbance average value exceeds the disturbance capacity, it results in causes the insensitive areas to shrink. At this point, the insensitive areas are unable to fill the entire TW_t space, resulting in significant changes to the distribution rule of ROSD. Consequently, there is a discrepancy between the actual experiment and the offline simulation results. Further inference indicates that as long as the disturbance average value affecting ROSD is below the disturbance capacity, the entire TW_t is equipped with robustness. Meanwhile, it is ensured that the distribution rule of ROSD in actual experiments is consistent with that in offline simulations. This insensitive area provides a theoretical basis for transferring offline simulation trajectory to underground environments. According to the experimental results, the extent of the insensitive area reaches its maximum when the mean disturbance approximates 500. Consequently, when the parameter settings are set in Tables 2 and 3 for UMCDPR, the disturbance capacity margin is 500, approximately. In this disturbance capacity, ROSD offline distribution rule closely matches the distribution rule in the underground environment. Since the end-effector in this article operates in a heavy-load environment, the estimated cumulative conversion of dynamic disturbances in the underground tunnel into end-effector disturbance forces does not exceed 100 [46], which is far less than the 500 considered in this article. Therefore, the index of ROSD allow for offline multi-trajectory optimization of the UMCDPR through an offline approach. In future research, the structural parameters of UMCDPR are also optimized based on insensitive areas to enhance the magnitude of these areas. However, this requires extensive experimentation to obtain accurate values for the disturbance capacity.

The task objective of UMCDPR is to transport loads from one assembling area to another. However, it is uncertain whether the UMCDPR moves from the negative x-axis to the positive x-axis or vice versa. According to the task objectives, sufficient stiffness needs to be achieved during the motion. Therefore, by guiding the UMCDPR to move along the ROSD, sufficient stiffness can be obtained. This determines the direction of motion, the initial area, and the termination area for the UMCDPR. Fig. 10 represents the x-coordinates cumulative sum of ROSD under different disturbance mean values. It can be observed that when the disturbance is less than ξ_3, the component of ROSD along the x-axis is significantly greater than 0. This indicates that a greater stiffness is achieved when moving from the negative half-axis of x to the positive half-axis of x. Therefore, we ultimately choose the assembling area pointed by the x-axis as the initial area, with the other assembling area serving as the terminal area, as well as confirming the movement direction of the UMCDPR.

To further illustrate the robustness advantages of ROSD, we compared ROSD with the state-of-the-art CDPR stiffness orientation selection methods. The relevant details are provided in Appendix B.

4.2. Verification of ROSD index and selection of multi-trajectory

After identifying the regions containing the initial and termination points, the next step is to select the optimal stiffness trajectory among all possible trajectories. Additionally, it is necessary to further confirm the correctness of using similarity measures to evaluate the stiffness of UMCDPR trajectories. To ascertain the relationship between similarity value and trajectory stiffness, we designed 20 sets of ROSD multi-trajectory optimization numerical simulations based on the characteristics of TW_t. The critical parameters across these 20 numerical simulations are compared, including total similarity, the number of sampling points, mean similarity, and total deformation. The results confirmed that the relationship between similarity value and system stiffness is consistent with the theoretical analysis. And a stiffness trajectory with a deformation not exceeding 0.027 m is obtained, within a safe distance.

4.2.1. Simulation steps

(1) Select a unit sphere with $\delta = 0.05$, and set UMCDPR movement speed to $\|\dot{\boldsymbol{p}}_j\| = 0.25$ m/s;

(2) Other relevant parameters are decided by values in Tables 1 to 3. Meanwhile, the experiment is conducted when the mean disturbance is set to ξ_3;

(3) As mentioned earlier, when the exact locations of the initial point and terminal point are unavailable, we choose a position that the UMCDPR must pass through within the TW_t space as the initial search point (*i.e.* the z-axis). As mentioned in Section 4.1.3, According to the ROSD distribution rule, it is evident that the points on the boundary of the area where $x > 0$ are chosen as the terminal points, while the points on the boundary of the area where $x < 0$ are selected as the initial points;

(4) Determine which trajectory exhibits the optimal stiffness according to Eq. (25). Additionally, assess whether the UMCDPR can collide with the mining hydraulic frame.

4.2.2. Simulation results

The experimental results are shown in Figs. 11–13, leading to two results:

(1) **Results of search with different initial points:** After completing the above experimental steps, a scatter plot with multi-trajectory is generated. To facilitate the observation of experimental results, B-spline curves are used to fit this scatter plot. The colors in Fig. 11 represent the trajectories obtained from selecting different initial search points. The results show that using point (0, 0, 1.1866) as the initial search point does not generate a valid trajectory. The initial search points of each trajectory are shown in Table 4. The initial search points of each trajectory are in Table 4.

Table 3
UMCDPR simulations parameters.

Name	Relevant parameters
The quality of hydraulic support m	6500kg
The maximum tension $\boldsymbol{T}_{max}$	40000N
The minimum tension $\boldsymbol{T}_{min}$	400N

(2) **Analysis of critical variable trends**: By the selected speed, it is determined that the time taken for each trajectory does not exceed 150 s. The trends of total trajectory similarity ΣS_j, the number of sampling points n_j, and mean similarity MSI are plotted as bar charts and line graphs, as shown in Fig. 12. Fig. 13 shows the maximum deformation of UMCDPR during movement. The mean similarity can be defined as

$$MSI = \frac{\sum_{j=1}^{n_j} S_j}{n_j}, i = 1, \cdots, 19 \tag{33}$$

where $j = 1, \dots n_j$. The method is provided for calculating the mean similarity, whose specific applications are in Section 4.2.3. Table 5 shows the two most significant results with the maximum deformation selected from 19 trajectory samples.

4.2.3. Discussion and analysis

For the practical task objectives of underground tunnel hoisting, we aim for UMCDPR to move from the negative of the x-axis to the positive while ensuring that the stiffness deformation of UMCDPR is minimized. Fortunately, the experiment results show that all 19 trajectory samples satisfy the task objectives. The possible reason that #20 does not generate a trajectory is that the point $\boldsymbol{p}_{j+1}$ with the maximum similarity is located outside the TW$_t$, resulting in no feasible points within TW$_t$. Therefore, the search terminates immediately under **Method 2**. When selecting points for search in task workspaces for other CDPRs, it is advisable to avoid choosing points near the boundary of task workspaces. Besides, the correctness of ROSD index is analyzed as follows:

To determine whether the similarity between ROSD and the motion direction of UMCDPR can function as a criterion for evaluating trajectory stiffness, the relationship between total similarity and total deformation, as defined by Eq. (29), needs to be taken into consideration. Based on Fig. 13, the total deformation $\Sigma||\Delta\boldsymbol{\varepsilon}_p||$ of UMCDPR at different initial positions and the corresponding total similarity for each trajectory are obtained. The change trends of both variables are presented in Fig. 14(a). Observations reveal that when the total similarity varies significantly among different trajectories, the total deformation trend aligns with the total similarity trend. For instance, there is a significant difference in total similarity between #1 and #2, as well as between #7, #8, #9, and #10. The trend in their total similarity aligns consistently with the trend in their total deformation. In contrast, when the differences in total similarity are small, the trend of total deformation is opposite to that of total similarity. For example, in the circled section of Fig. 14(a), the trend in total similarity is opposite to the trend in total deformation. According to previous conclusions, greater similarity corresponds to smaller deformation. However, partial trends in Fig. 14(a) contradict this conclusion. The reason is that when total

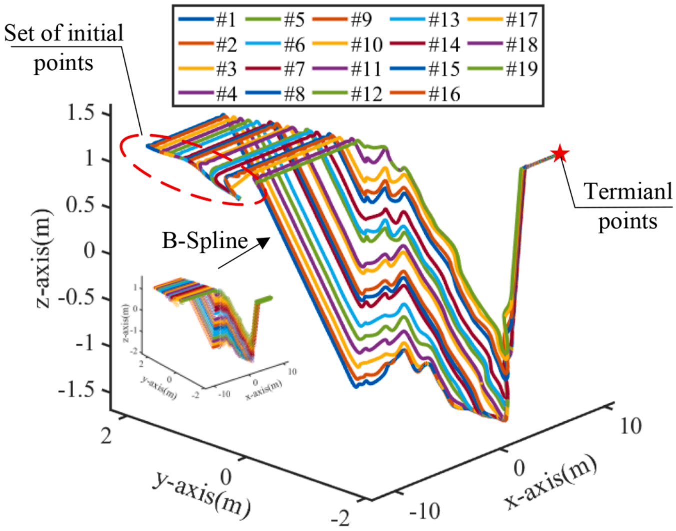

Fig. 11. Experimental results with different initial points. The trajectory IDs are numbered from bottom to top, with 19 samples. The initial search points for each trajectory are shown in Table 4.

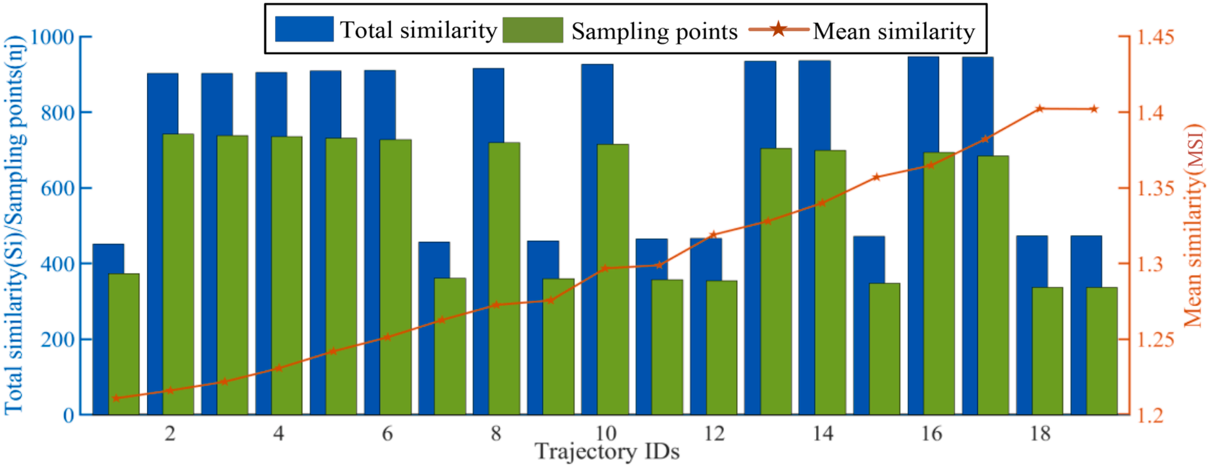

Fig. 12. Trend of critical variables. Bar chart values follow the blue left axis, and line chart values follow the red right axis.

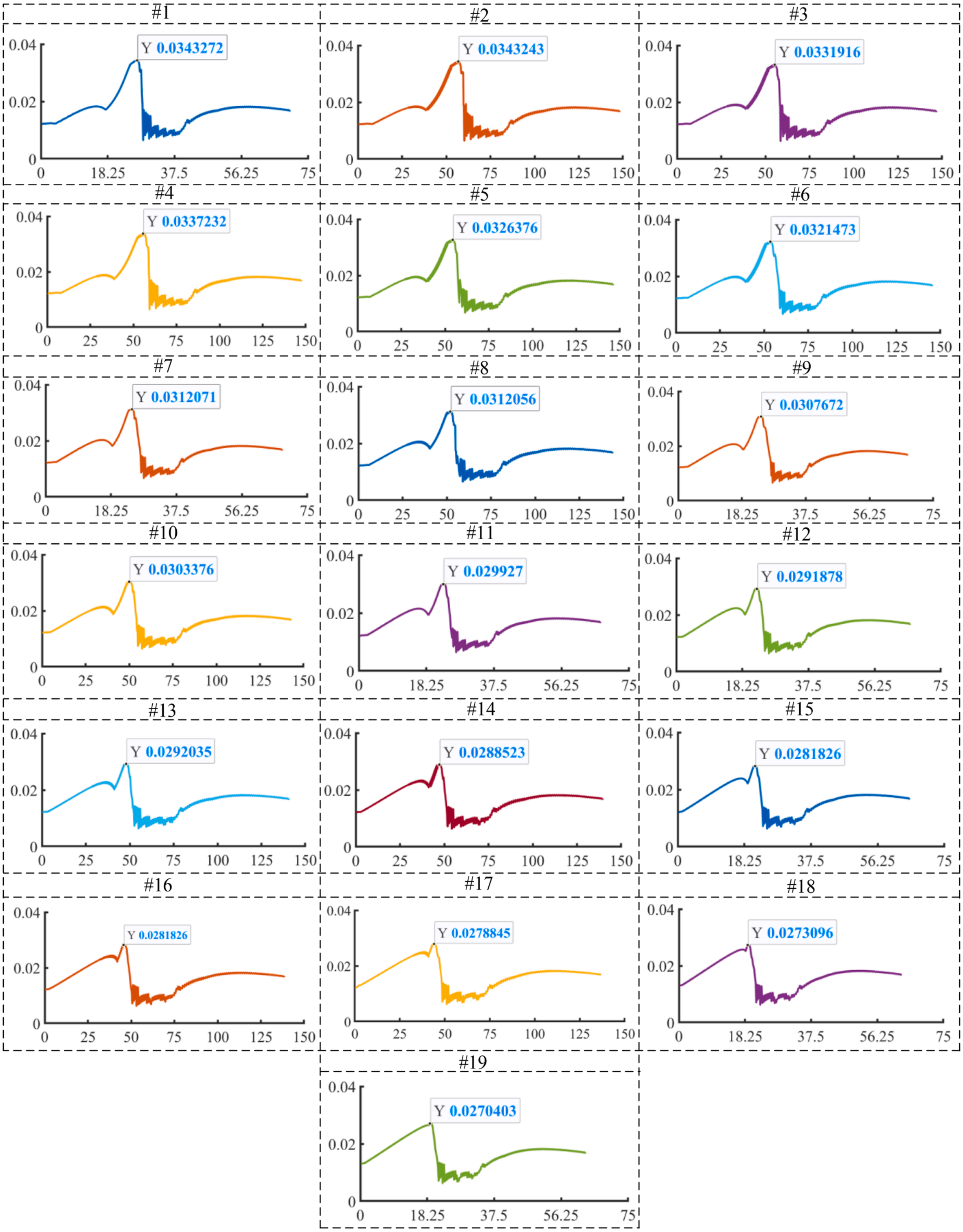

Fig. 13. Trend of deformation changes in UMCDPR. The numerical value in Fig. 7 indicates the maximum deformation amount for UMCDPR. The horizontal axis represents the motion time, and the vertical axis represents the motion deformation. The colors in the figure are consistent with those in Fig. 11.

Table 4

Corresponding initial search points for different trajectory IDs.

IDs	#1	#2	#3	#4	#5
Initial point	(0, 0, -1.5000)	(0, 0, -1.3586)	(0, 0, -1.2172)	(0, 0, -1.0758)	(0, 0, -0.9344)
IDs	#6	#7	#8	#9	#10
Initial point	(0, 0, -0.7930)	(0, 0, -0.6516)	(0, 0, -0.5102)	(0, 0, -0.3688)	(0, 0, -0.2274)
IDs	#11	#12	#13	#14	#15
Initial point	(0, 0, -0.0860)	(0, 0, 0.0544)	(0, 0, 0.1968)	(0, 0, 0.3382)	(0, 0, 0.4796)
IDs	#16	#17	#18	#19	None
Initial point	(0, 0, 0.6210)	(0, 0, 0.7624)	(0, 0, 0.9038)	(0, 0, 1.0452)	(0, 0, 1.1866)

Table 5

The IDs of two trajectory samples with the largest and smallest maximum deformation values.

IDs	The number of sampling points (n_j)	Total similarity ($\sum_{j=1}^{n_j} S_j$)	Total deformation ($\sum_{j=1}^{n_j} \| \Delta\varepsilon_j \|$)	Mean similarity (*MSI*)	Maximum deformation (max $\Delta\boldsymbol{\varepsilon}_p$)
#2	742	902.352	1.242	1.216	0.034
#19	337	472.487	0.555	1.402	0.027

similarity values differ significantly, the number of sampling points for UMCDPR shows significant differences across different trajectories. Thus, the accumulation of similarity exhibits notable differences due to substantial variations in sampling points. In other words, when the number of sampling points varies significantly, UMCDPR accumulates a much higher total similarity, which obscures the relationship between total similarity and total deformation. Accordingly, this leads to a trend that contradicts our theoretical results.

Conversely, when the difference in the number of sampling points is relatively small, the true trend based on the total deformation and total similarity of ROSD becomes increasingly evident. Therefore, the significant difference in the total similarity is primarily attributed to the substantial difference in the number of sampling points of UMCDPR across different trajectories. When the difference in total similarity is relatively small, it suggests that the impact of the number of sampling points in UMCDPR on enhancing the total similarity is minor, making the influence of ROSD in the simulation unmasked. The trends circled in Fig. 14(a) illustrate that when the differences in different trajectory total similarities are small, the total deformation trends in the opposite direction to the total similarity. This observation validates the correctness of the ROSD trajectory method.

Calculating only the total similarity is insufficient to determine the quality of trajectory stiffness, according to Fig. 10(a). Based on the above analysis, we understand that significant differences in the number of sampling points can lead to substantial deviations in assessing trajectory stiffness using total similarity. Therefore, the mean similarity is considered as the criterion for evaluation. The maximum deformation and the mean similarity of 19 trajectory samples are plotted as a line graph, as shown in Fig. 14(b). At the beginning of Section 3.2, we analyzed that max $\boldsymbol{K}_p \Leftrightarrow \min \Delta\boldsymbol{\varepsilon}$. Similarly, min $\boldsymbol{K}_p \Leftrightarrow \max \Delta\varepsilon$. This graph shows that mean similarity is inversely proportional to maximum deformation. As the mean similarity increases, the deformation during UMCDPR's movement from $\boldsymbol{p}_j$ to $\boldsymbol{p}_{\mathrm{j}+1}$ becomes smaller. A smaller maximum deformation indicates better trajectory stiffness, according to the analysis results of Section 3.2. Therefore, mean similarity can be a criterion for selecting the optimal stiffness among multi-trajectory.

The highest mean similarity occurs at #18 and #19, indicating that the trajectories corresponding to these points have the greatest stiffness and the smallest maximum deformation, as shown in Fig. 14(b). According to the equation that max $\boldsymbol{K}_p \Leftrightarrow \min \Delta\boldsymbol{\varepsilon}$, the trajectory with the shortest time and smallest maximum deformation is selected. Ultimately, #19 is chosen with a maximum deformation of 0.027 m.

According to the second task objective, the UMCDPR must not collide with the mining hydraulic frame. Based on Table 1, the minimum distance between TW_t and the mining hydraulic frame is 0.5 m, and 0.027 m << 0.5 m, so UMCDPR does not collide with the mining hydraulic frame during its movement.

5. Conclusion

This research primarily proposes the offline multi-trajectory optimization index, ROSD, for UMCDPR, which exhibits three critical characteristics: (1) This index can select the trajectory with the optimal stiffness from multiple possible trajectories. (2) When the actual disturbance mean does not exceed the disturbance capacity, ROSD retains most distribution rules, indicating strong robustness. (3) The distribution rules of this index within TW_t are globally visible. The significance of this index lies in the fact that the generated optimal stiffness trajectories are equally reliable and plausible even in a strong disturbance environment. Based on this research, the following application values can be drawn:

(1) From a safety perspective, within the threshold of disturbance capacity, the ROSD index ensures the invariance of the distribution rule in offline simulations. This allows for multi-trajectory optimization through offline simulations, with results that are more reliable compared to other stiffness optimization indices.
(2) The ROSD offline multi-trajectory optimization method is capable of addressing engineering problems with relatively ambiguous task objectives. It standardizes the underground assembly trajectories, ensuring personal safety.

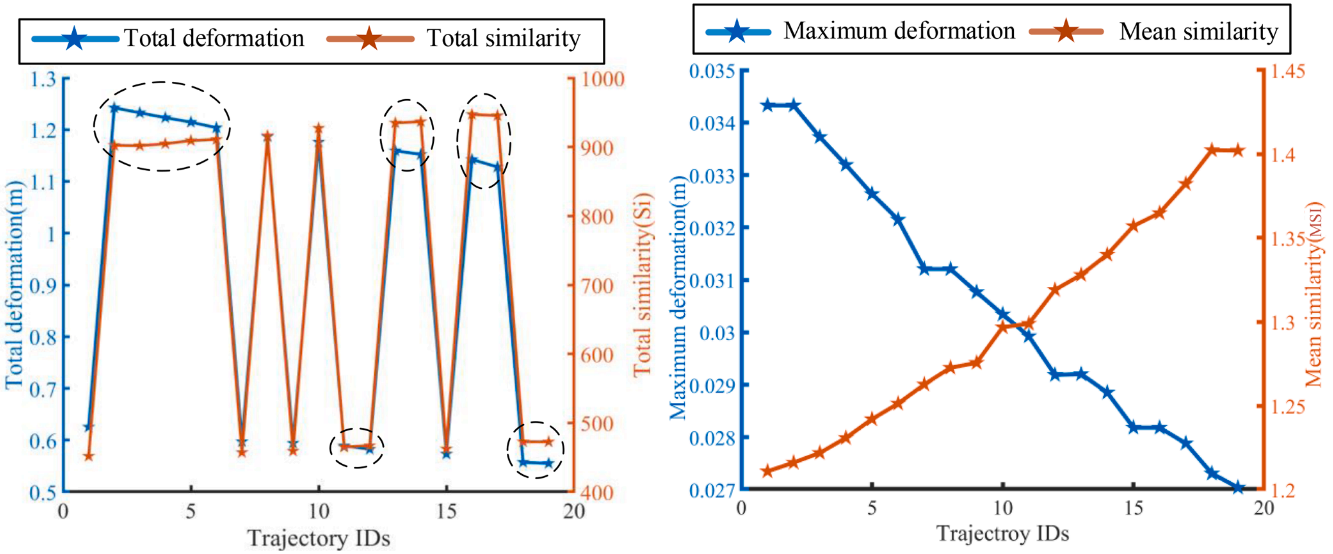

Fig. 14. Comparison of deformation and similarity trends: (a) The trends in total deformation and total similarity. (b) The trends in maximum deformation and mean similarity. The blue line corresponds to the blue vertical axis and the red line corresponds to the red axis.

(3) The mean similarity, which serves as a performance index for evaluating the stiffness of robotic trajectories, establishes a new criterion for assessing stiffness across multi-trajectory.

This index is equally suitable for other CDPRs and introduces ROSD for assessing multi-trajectory stiffness, marking a pioneering effort. In future research, the core objective will be to rigorously test the ROSD framework through various operational requirements of CDPR systems, eventually seeking to generalize and refine the multi-trajectory optimization method pertinent to ROSD applications.

CRediT authorship contribution statement

Weihan Jia: Writing – original draft, Visualization, Validation, Software, Methodology, Investigation, Formal analysis, Data curation, Conceptualization. **Gang Cheng:** Writing – review & editing, Validation, Supervision, Project administration, Investigation, Funding acquisition, Conceptualization. **Jun Li:** Writing – review & editing, Software, Investigation, Conceptualization. **Yusong Pang:** Validation, Supervision, Investigation. **Mengyao Hu:** Writing – original draft, Software, Investigation. **Wei Gu:** Validation, Supervision, Investigation.

Declaration of competing interest

The authors declare that they have no known competing financial interests or personal relationships that could have appeared to influence the work reported in this paper.

The authors declare the following financial interests/personal relationships which may be considered as potential competing interests:

Acknowledgment

This study was supported by the Postgraduate Research & Practice Innovation Program of Jiangsu Province with grant No. KYCX24_2717 and the Graduate Innovation Program of China University of Mining and Technology with grant No. 2024WLKXJ073. The authors wish to thank the National Nature Science Foundation of China (NSFC) with grant No. 52275039.

Appendix A

The kinematic equations for UMCDPR can be formulated as

$$A_iB_i = \boldsymbol{c}_i = \boldsymbol{p} + \boldsymbol{R} \cdot \boldsymbol{b}_i - \boldsymbol{a}_i \tag{A.1}$$

The pulley coordinate system A_i-$\boldsymbol{x}_{ri}\boldsymbol{y}_{ri}\boldsymbol{z}_{ri}$ is fixed to the pulley. $\boldsymbol{z}_{ri}$ along the pulley's rotation axis. Unit vector $\boldsymbol{y}_{ri}$ is parallel to the direction of A_iE_i. The direction of $\boldsymbol{x}_{ri}$ is determined by the right-hand rule. According to the notation used in [47], the coordinates $\boldsymbol{x}_{ri}$, $\boldsymbol{y}_{ri}$, $\boldsymbol{z}_{ri}$ can be expressed in terms of the global coordinates $\boldsymbol{x}$, $\boldsymbol{y}$, $\boldsymbol{z}$ as follows:

$$\boldsymbol{z}_{ri} = \boldsymbol{z}, \quad \boldsymbol{x}_{ri} = -\boldsymbol{x}\sin\theta_i - \boldsymbol{y}\cos\theta_i, \quad \boldsymbol{y}_{ri} = \boldsymbol{x}\cos\theta_i - \boldsymbol{y}\sin\theta_i \tag{A.2}$$

where

$$\theta_i = \arctan\left(\frac{\left(\boldsymbol{p} + \boldsymbol{R}\cdot\boldsymbol{b}_i\right)^T \cdot (1,\ 0,\ 0)^T}{\left(\boldsymbol{p} + \boldsymbol{R}\cdot\boldsymbol{b}_i\right)^T \cdot (0,\ 1,\ 0)^T}\right)$$

According to the geometric relationship of the pulley motion, C_i, D_i, and B_i always remain on the same plane, with B_i being the point of tangency, as follows:

$$\boldsymbol{c}_i = h\boldsymbol{y}_{ri} + r\boldsymbol{u}_{ri} + l_i\boldsymbol{u}_i \tag{A.3}$$

where l_i is the length of the cable. $\boldsymbol{u}_{ri}$ and $\boldsymbol{u}_i$ are the unit vector directions of E_iC_i and l_i, respectively. In the coordinate system A_i-$x_{ri}y_{ri}z_{ri}$, $\boldsymbol{u}_i$ and $\boldsymbol{u}_{ri}$ can be expressed as

$$\boldsymbol{u}_{ri} = \boldsymbol{y}_{ri}\cos\varphi_i + \boldsymbol{z}_{ri}\sin\varphi_i, \quad \boldsymbol{u}_i = \boldsymbol{y}_{ri}\sin\varphi_i - \boldsymbol{z}_{ri}\cos\varphi_i \tag{A.4}$$

By taking the dot product of Eq. (A.3) with $\boldsymbol{u}_{ri}$, the solution can be depicted as

$$(\boldsymbol{y}_{ri}\cos\varphi_i + \boldsymbol{z}_{ri}\sin\varphi_i) \cdot \boldsymbol{c}_i = r - h\cos\varphi_i \tag{A.5}$$

The φ_i can be formulated as

$$\varphi_i = 2\arctan\left(\frac{h + \boldsymbol{y}_{ri}\cdot\boldsymbol{c}_i}{r + \boldsymbol{z}_{ri}\cdot\boldsymbol{c}_i} + \sqrt{\left(\frac{h + \boldsymbol{y}_{ri}\cdot\boldsymbol{c}_i}{r + \boldsymbol{z}_{ri}\cdot\boldsymbol{c}_i}\right)^2 + \frac{r - \boldsymbol{z}_{ri}\cdot\boldsymbol{c}_i}{r + \boldsymbol{z}_{ri}\cdot\boldsymbol{c}_i}}\right) \tag{A.6}$$

To determine the velocity and acceleration of UMCDPR, Eqs. (A.1) and (A.3) are combined and then differentiated concerning time as follows:

$$\dot{\boldsymbol{l}}_i = \dot{\boldsymbol{p}} + \boldsymbol{\omega} \times \boldsymbol{b}_i - h\dot{\boldsymbol{y}}_{ri} + r\dot{\boldsymbol{u}}_{ri} \tag{A.7}$$

where $\boldsymbol{\omega}$ represents the angular velocity of UMCDPR, and differentiating Eq. (A.2) for time gives:

$$\dot{\boldsymbol{x}}_{ri} = -\boldsymbol{y}_{ri} \cdot \dot{\theta}_i, \quad \dot{\boldsymbol{y}}_{ri} = \boldsymbol{x}_{ri} \cdot \dot{\theta}_i \tag{A.8}$$

Since points A_i and B_i lie on the same plane, $\boldsymbol{x}_{ri}$ is always perpendicular to the plane. We have $\boldsymbol{x}_{ri}\cdot(\boldsymbol{p} + \boldsymbol{b}_i - \boldsymbol{a}_i) = 0$, taking the derivative of this equation as follows:

$$\dot{\boldsymbol{x}}_{ri} \cdot (\boldsymbol{p} + \boldsymbol{R} \cdot \boldsymbol{b}_i - \ - \boldsymbol{a}_i) + \boldsymbol{x}_{ri} \cdot (\dot{\boldsymbol{p}} + \boldsymbol{\omega} \times \boldsymbol{b}_i) = 0 \tag{A.9}$$

Substituting Eq. (A.8) into Eq. (A.9) can be solved as

$$\dot{\theta}_i = \frac{\boldsymbol{x}_{ri} \cdot (\dot{\boldsymbol{p}} + \boldsymbol{\omega} \times \boldsymbol{b}_i)}{\boldsymbol{y}_{ri} \cdot \boldsymbol{c}_i} \tag{A.10}$$

For equation Eq. (A.7), $\boldsymbol{u}_{ri}$ is still unknown. Let's now find the expression for $\boldsymbol{u}_{ri}$. Firstly, Eq. (A.4) is differentiated concerning time. Since $\boldsymbol{z}_{ri}$ is constant and does not change with time, the derivative of $\boldsymbol{u}_{ri}$ can be described as

$$\dot{\boldsymbol{u}}_{ri} = \dot{\boldsymbol{y}}_{ri}\cos\varphi_i - \boldsymbol{u}_i \cdot \dot{\varphi}_i \tag{A.11}$$

Secondly, differentiate Eq. (A.5) for time, and substitute Eq. (A.11) with it. This allows us to solve for

$$\dot{\varphi} = \frac{2\boldsymbol{y}_{ri} \cdot (\dot{\boldsymbol{p}} + \boldsymbol{\omega} \times \boldsymbol{b}_i)\cos\varphi_i}{(\boldsymbol{y}_{ri} \cdot \boldsymbol{c}_i + h)\sin\varphi_i} \tag{A.12}$$

Finally, by combining equations Eqs. (A.7), (A.8), (A.10)–(A.12), the velocity equation along cable can be solved as

$$\dot{\boldsymbol{l}}_i = \dot{\boldsymbol{p}} + \boldsymbol{\omega} \times \boldsymbol{b}_i + \frac{r\cos\varphi_i - h}{\boldsymbol{y}_{ri} \cdot \boldsymbol{c}_i}(\dot{\boldsymbol{p}} + \boldsymbol{\omega} \times \boldsymbol{b}_i) + \frac{2\cos\varphi_i}{\boldsymbol{y}_{ri} \cdot \boldsymbol{c}_i + h}(\dot{\boldsymbol{p}} + \boldsymbol{\omega} \times \boldsymbol{b}_i) \tag{A.13}$$

Appendix B

This article selects other indices describing CDPR stiffness orientations for robustness comparisons. The mathematical formulations of the optimal stiffness selection methods described in [30,41], and [48] can be expressed as

$$\max \quad C(S) = \frac{\lambda_{\max}^2 \lambda_{\min}^2}{\lambda_{\min}^2 + \lambda_{\min}^2} \tag{B.1}$$

where, $\lambda_{\max}$and$\lambda_{\min}$denote the maximum and minimum eigenvalues of the stiffness matrix. When the value of $C(S)$ is maximized, the corresponding stiffness matrix is considered the optimal stiffness matrix, and the eigenvector corresponding to its maximum eigenvalue represents the optimal stiffness orientation.

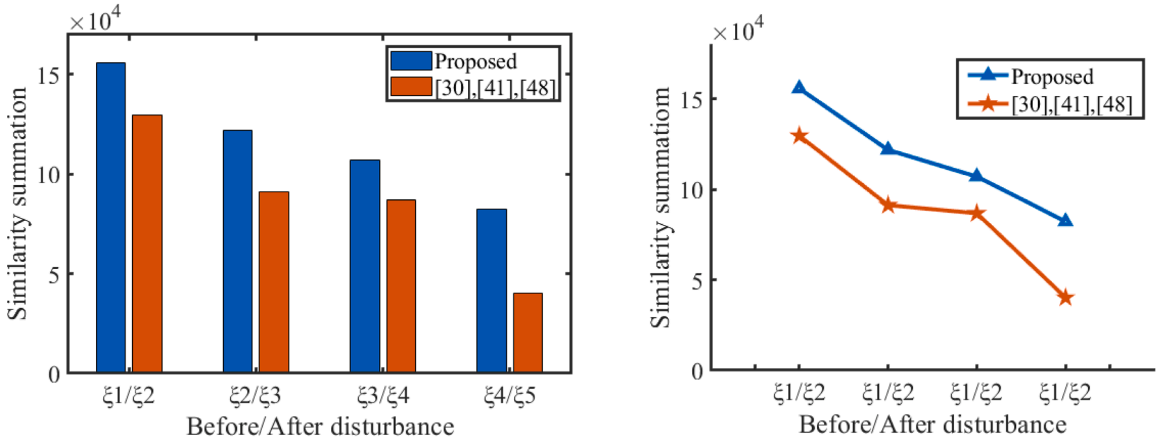

Fig. 15. Comparison of total similarity between ROSD and other indices.

According to the methods described in Refs. [30,41,48], we derived the optimal stiffness orientations for all sampling points in TW_t. Under the condition that the ξ_1, ξ_2, ξ_3, ξ_4, ξ_5 are kept the same as the parameters in this article, we calculated the total similarity before and after applying different disturbances to all sampling points in TW_t and compared it with the ROSD proposed in this article, as shown in Fig. 15. The total directional similarity of ROSD is greater than that of the index selected from Refs. [30,41,48], demonstrating that the optimal stiffness orientations selected by the method proposed in this article are more robust. Furthermore, both indices show a decreasing trend in total similarity as the mean disturbance increases, which validates the rationality of the total similarity criteria used in the simulations.

Data availability

Data will be made available on request.

References

[1] G. Wang, H. Ren, Y. Pang, et al., Research and engineering progress of intelligent coal mine technical system in early stages, Int. J. Coal. Sci. Technol. 48 (7) (2020) 1–27, https://doi.org/10.13199/j.cnki.cst.2020.07.001.

[2] G. Wang, H. Ren, G. Zhao, et al., Research and practice of intelligent coal mine technology systems in China, Int. J. Coal. Sci. Technol. 9 (2022) 24, https://doi.org/10.1007/s40789-022-00491-3.

[3] B. Zhang, B. Deng, X. Gao, Design and implementation of fast terminal sliding mode control with synchronization error for cable-driven parallel robots, Mech. Mach. Theory 182 (2023) 105228, https://doi.org/10.1016/j.mechmachtheory.2023.105228.

[4] N. Zhang, W. Shang, Dynamic trajectory planning of a 3-DOF under-constrained cable-driven parallel robot, Mech. Mach. Theory 98 (2016) 21–35, https://doi.org/10.1016/j.mechmachtheory.2015.11.007.

[5] Z. Cui, X. Tang, Analysis of stiffness controllability of a redundant cable-driven parallel robot based on its configuration, Mechatronics 75 (2021) 102519, https://doi.org/10.1016/j.mechatronics.2021.102519.

[6] J. Yu, J. Tao, G. Wang, et al., Stability analysis and optimal design of a cable-driven parallel robot, Rob. Auton. Syst. 173 (2024) 104611, https://doi.org/10.1016/j.robot.2023.104611.

[7] H. Jamshidifar, A. Khajepour, B. Fidan, et al., Kinematically-constrained redundant cable-driven parallel robots: modeling, redundancy analysis, and stiffness optimization, IEEE/ASME Trans. Mechatron 22 (2) (2017) 921–930, https://doi.org/10.1109/TMECH.2016.2639053.

[8] H. Yuan, E. Courteille, D. Deblaise, et al., Static and dynamic stiffness analyses of cable-driven parallel robots with non-negligible cable mass and elasticity, Mech. Mach. Theory 85 (2015) 64–81, https://doi.org/10.1016/j.mechmachtheory.2014.10.010.

[9] C. Charlie, Disturbance of mining operations to a deep underground workshop, Tunn. Unn. Undergr. Sp. Tech. 21 (2006) 1–9, https://doi.org/10.1016/j.tust.2005.04.001.

[10] H. Yang, C. Han, N. Zhang, et al., Stability control of a goaf-side roadway under the mining disturbance of an adjacent coal working face in an underground mine, Sustainability 11 (2019) 6398, https://doi.org/10.3390/su11226398.

[11] N. Agarwal, B. Bullins, E. Hazan, et al., Online control with adversarial disturbances, in: Proceedings of the International Conference on Machine Learning, 2019, pp. 111–119, https://doi.org/10.48550/arXiv.1902.08721.

[12] Q. Qian, P. Lin, Safety risk management of underground engineering in China: progress, challenges and strategies, J. Rock Mech. Geotech. 8 (4) (2016) 423–442, https://doi.org/10.1016/j.jrmge.2016.04.001.

[13] G. Sun, Z. Liu, H. Gao, et al., Available wrench set robustness under hybrid joint-space control to uncertain wrench for a cable-driven parallel robot, Mech. Mach. Theory 194 (2024) 105568, https://doi.org/10.1016/j.mechmachtheory.2023.105568.

[14] H. Gao, G. Sun, Z. Liu, et al., Tension distribution algorithm based on graphics with high computational efficiency and robust optimization for two-redundant cable-driven parallel robots, Mech. Mach. Theory 172 (2022) 104739, https://doi.org/10.1016/j.mechmachtheory.2022.104739.

[15] V. Portman, V. Chapsky, Robot stiffness theory reconsideration based on schur complement eigenvalues: extension to GSP dynamic stiffness evaluation, Mech. Mach. Theory 184 (2023) 105257, https://doi.org/10.1016/j.mechmachtheory.2023.105257.

[16] V. Nguyen, C. Kuo, P. Lin, Compliance error compensation of a robot end-effector with joint stiffness uncertainties for milling: an analytical model, Mech. Mach. Theory 170 (2022) 104717, https://doi.org/10.1016/j.mechmachtheory.2021.10471.

[17] Q. Cheng, W. Xu, Z. Liu, et al., Optimal trajectory planning of the variable-stiffness flexible manipulator based on CADE algorithm for vibration reduction control, Front. Bioeng. Biotechnol. 9 (2021) 766495, https://doi.org/10.3389/fbioe.2021.766495.

[18] J. Zhao, Y. Duan, B. Xie, et al., FSW robot system dimensional optimization and trajectory planning based on soft stiffness indices, J. Manuf. Process. 63 (2021) 88–97, https://doi.org/10.1016/j.jmapro.2020.05.004.

[19] M. Posa, R. Tedrake, Direct trajectory optimization of rigid body dynamical systems through contact, in: Proceedings of the Algorithmic Foundations of Robotics X: Proceedings of the Tenth Workshop on the Algorithmic Foundations of Robotics, Berlin, Heidelberg, Springer Berlin Heidelberg, 2013, pp. 527–542. https://link.springer.com/chapter/10.1007/978-3-642-36279-8_32.

[20] W. Li, X. Yang, C. Lu, et al., Modeling and optimization of trajectory deviation for compound directional drilling in coal mines, Neurocomputing 618 (2025) 129029, https://doi.org/10.1016/j.neucom.2024.129029.

[21] L. Barbazza, F. Oscari, S. Minto, et al., Trajectory planning of a suspended cable-driven parallel robot with reconfigurable end-effector, Robot. Comput. Integr. Manuf. 48 (2017) 1–11, https://doi.org/10.1016/j.rcim.2017.02.001.

[22] Y. Sun, Y. Guo, C. Song, et al., Wrench-feasible workspace-based design of hybrid thruster and cable-driven parallel robots, Mech. Mach. Theory 172 (2022) 104758, https://doi.org/10.1016/j.mechmachtheory.2022.104758.

[23] M. Badrikouhi, M. Bamdad, Design, modeling, implementation, and trajectory planning of a 3-DOF cable-driven parallel robot, Appl. Math. Model. 125 (2024) 210–229, https://doi.org/10.1016/j.apm.2023.09.018.

[24] X. Jin, W. Ye, Q. Li, New indices for performance evaluation of cable-driven parallel robots: motion/force transmissibility, Mech. Mach. Theory 188 (2023) 105402, https://doi.org/10.1016/j.mechmachtheory.2023.105402.

[25] S. Liu, J. Mei, P. Wang, et al., Optimal design of a coupling-input cable-driven parallel robot with passive limbs based on force space analysis, Mech. Mach. Theory 184 (2023) 105296, https://doi.org/10.1016/j.mechmachtheory.2023.105296.

[26] Q. Meng, F. Xie, R. Tang, et al., Deployable polyhedral mechanisms with radially reciprocating motion based on novel basic units and an additive-then-subtractive design strategy, Mech. Mach. Theory 181 (2023) 104174, https://doi.org/10.1016/j.mechmachtheory.2022.105174.

[27] B. Kosko, Fuzzy Engineering, Prentice-Hall, Inc, 1996. https://dl.acm.org/doi/abs/10.5555/241678.

[28] J. Mockus, W. Eddy, G. Reklaitis, Bayesian Heuristic Approach to Discrete and Global Optimization: Algorithms, Visualization, Software, and Applications, Springer Science & Business Media, 2013, 17, https://link.springer.com/book/10.1007/978-1-4757-2627-5.

[29] Z. Cui, X. Tang, S. Hou, Research on controllable stiffness of redundant cable-driven parallel robots, IEEE/ASME Trans. Mechatron. 23 (5) (2018) 2390–2401, https://doi.org/10.1109/TMECH.2018.2864307.

[30] A. Alamdari, R. Haghighi, V. Krovi, Stiffness modulation in an elastic articulated-cable leg-orthosis emulator: theory and experiment, IEEE Trans. Robot. 34 (5) (2018) 1266–1279, https://doi.org/10.1109/TRO.2018.2830356.

[31] X. Ge, J. Xie, X. Wang, et al., A virtual adjustment method and experimental study of the support attitude of hydraulic support groups in propulsion state, Measurement 158 (2020) 107743, https://doi.org/10.1016/j.measurement.2020.107743.

[32] T. Zeng, Y. Meng, H. Zhou, Analysis on the pose and dynamic response of hydraulic support under dual impact loads, Int. J. Simul. Model. 17 (2018), 69-8, https://www.ijsimm.com/Full_Articles/Fulltext2018/text17-1_69-80.pdf.

[33] F. Xie, W. Shang, B. Zhang, et al., High-precision adaptive control of cable-driven parallel robots with convergence guarantee, IEEE Trans. Industr. Inform. 17 (2021) 2488–2498, https://doi.org/10.1109/TIE.2023.3310012.

[34] W. Shang, B. Zhang, S. Cong, et al, Dual-space adaptive synchronization control of redundantly-actuated cable-driven parallel robots, 152 (2020) 103954. 10.1016/j.mechmachtheory.2020.103954.

[35] Pott Andreas, Cable-Driven Parallel Robots. Ed. Tobias Bruckmann, Springer, Berlin/Heidelberg, Germany, 2013.

[36] Z. Zhang, G. Xie, Z. Shao, et al., Kinematic calibration of cable-driven parallel robots considering the pulley kinematics, Mech. Mach. Theory 169 (2022) 104648, https://doi.org/10.1016/j.mechmachtheory.2021.104648.

[37] A. Gonzalez-Rodriguez, F. Castillo-Garcia, E. Ottaviano, et al., On the effects of the design of cable-driven robots on kinematics and dynamics models accuracy, Mechatronics 43 (2017) 18–27, https://doi.org/10.1016/j.mechatronics.2017.02.002.

[38] T. Paty, N. Binaud, S. Caro, et al., Cable-driven parallel robot modelling considering pulley kinematics and cable elasticity, Mech. Mach. Theory 159 (2021) 104263, https://doi.org/10.1016/j.mechmachtheory.2021.104263.

[39] M. Khosravi, H. Taghirad, Robust PID control of fully-constrained cable-driven parallel robots, Mechatronics 24 (2014) 87–97, https://doi.org/10.1016/j.mechatronics.2013.12.001.

[40] Z. Liao, Q. Wang, H. Xie, et al., Optimization of robot posture and workpiece setup in robotic milling with stiffness threshold, IEEE/ASME Trans. Mechatron. 27 (1) (2022) 1083–4435, https://doi.org/10.1109/TMECH.2021.3068599.

[41] X. Zhou, S. Jun, V. Krovi, Stiffness modulation exploiting configuration redundancy in mobile cable robots, in: Proceedings of the IEEE International Conference on Robotics and Automation, 2014, pp. 5934–5939, https://doi.org/10.1109/ICRA.2014.6907733.

[42] H. Gao, G. Sun, Z. Liu, et al., Tension distribution algorithm based on graphics with high computational efficiency and robust optimization for two-redundant cable-driven parallel robots, Mech. Mach. Theory 172 (2022) 104739, https://doi.org/10.1016/j.mechmachtheory.2022.104739.

[43] S. Bouchard, C. Gosselin, B. Moore, On the ability of a cable-driven robot to generate a prescribed set of wrenches, ASME. J. Mech. Robot. 2 (1) (2010) 011010, https://doi.org/10.1115/1.4000558.

[44] T. Hales, A proof of the Kepler conjecture, Ann. Math. 162 (3) (2005) 1065–1185, https://doi.org/10.48550/arXiv.1501.02155.

[45] T. Hales, A Formal Proof of the Kepler Conjecture, Forum of Mathematics Pi, 2017, https://doi.org/10.1017/fmp.2017.1.

[46] F. Feng, S. Chen, X. Zhao, et al., Effects of external dynamic disturbances and structural plane on rock fracturing around deep underground cavern, Int. J. Coal Sci. Technol. 9 (1) (2022) 15, https://doi.org/10.1007/s40789-022-00487-z.

[47] S. Guo, G. Wang, Z. Qi, et al., A quasi-static model for kinematic analysis of a feed driving mechanism, Mech. Mach. Theory 148 (2020) 103780, https://doi.org/10.1016/j.mechmachtheory.2020.103780.

[48] S. Yeo, G. Yang, W. Lim, Design and analysis of cable-driven manipulators with variable stiffness, Mech. Mach. Theory 69 (2013) 230–244, https://doi.org/10.1016/j.mechmachtheory.2013.06.005.